Rodrigo Filipe Leite Rendeiro

Design de componentes de um sistema ótico para aplicação em LiDAR automotivo
Design of optical system components for automotive LiDAR applications

Rodrigo Filipe Leite Rendeiro

Design de componentes de um sistema ótico para aplicação em LiDAR automotivo
Design of optical system components for automotive LiDAR applications

Dissertação apresentada à Universidade de Aveiro para cumprimento dos requisitos necessários à obtenção do grau de Mestre em Engenharia Física, realizada sob a orientação científica do Doutor Carlos Alberto Ferreira Marques, Professor auxiliar do Departamento de Física da Universidade de Aveiro, e do Doutor Ricardo Xavier da Graça Ferreira, líder da equipa de hardware na LiangDao GmbH.

Internship report presented to the University of Aveiro to fulfil the necessary requirements for the Master's Degree in Engineering Physics, held under the scientific guidance of PhD Carlos Alberto Ferreira Marques, Auxiliar Professor at the Department of Physics of the University of Aveiro, and of PhD Ricardo Xavier da Graça Ferreira, Teamlead of the Hardware Team at LiangDao GmbH.

o júri / the jury

Presidente   **Doutora Teresa Maria Fernandes Rodrigues Cabral Monteiro**
Professor Associado com agregação do Departamento de Física da Universidade de Aveiro

Arguente   **Doutor Paulo Sérgio De Brito André**
Professor Catedrático do Instituto Superior Técnico, Universidade de Lisboa

Orientador   **Doutor Carlos Alberto Ferreira Marques**
Professor Auxiliar do Departamento de Física da Universidade de Aveiro

agradecimentos / acknowledgements

Começo por agradecer aos meus orientadores, Professor Carlos Marques e Doutor Ricardo Ferreira por todo o conhecimento, disponibilidade e paciência que me dedicaram. Obrigado por confiarem em mim e me terem permitido um trabalho autónomo ao longo de toda a tese. Agradeço novamente ao meu co-orientador Doutor Ricardo Ferreira e ao professor Luís Rino, por me sugerirem a aventura de desenvolver o tema para a escrita da tese em contexto empresarial no estrangeiro, que foi uma oportunidade para crescimento pessoal e profissional. Agradeço a todos os professores que ao longo do meu percurso académico me ajudaram, desde a escola primária até à conclusão deste ciclo de estudos. Um especial obrigado a todos os professores do DFIS e associados que ao longo desta jornada me prepararam e ensinaram as ferramentas necessárias para resolver os meus problemas. Agradeço a todos os amigos que se cruzaram comigo ao longo desta jornada. Obrigado aos meus veteranos, Aparas, Cagarro, Reimão, Jason e Panados. Obrigado aos amigos que partilharam comigo o ano de caloiro e me ajudaram a criar memórias que carregarei para o resto da minha vida. Obrigado Prata, Azevedo, Gordo, Ricardo, Samuel, Bessa, Solla, Gui e Tardego. Obrigado às minhas meninas Teresa, Rita, Gusta, Margarida, Sofia e Camila. Obrigado aos meus aluviõezinhos Miguel, Rita, Tó, Daniel e Catarina. Obrigado pelas horas que todos vós perderam a aturar este teimoso. Com todos vocês ri, chorei e cresci. Um muito obrigado por todos os momentos de sobriedade (e intoxicação) que partilhamos e que fizeram de Aveiro a nossa casa e segunda família. A fotossíntese e a biblioteca vão sentir a nossa falta. Obrigado a todos os meus amigos da bandinha e amigos da terrinha, Tiago, Zé Órfão, Mató e Eugénio, que entre todas as outras coisas, me permitiram manter em forma em épocas de pausa. Agradeço à vida que todos os dias sorri para mim e me dá tantos desafios para resolver e razões para viver. Agradeço à Física por me ensinar a olhar de forma diferente para o mundo. Por fim mas acima de tudo, agradeço aos meus pais e avós pelo apoio dado ao longo de toda vida. Obrigado por depositarem em mim a vossa confiança e me permitirem voar mais alto. "(...) The aeroplane and the radio have brought us closer together. The very nature of these inventions cries out for the goodness in men - cries out for universal brotherhood - for the unity of us all. (...) Let us fight for a world of reason, a world where science and progress will lead to all men's happiness." In "The Great Dictator" by Charlie Chaplin, 1940.

LiangDao GmbH is a Sino-German company focused on LiDAR-based solutions for applications in Automotive and Smart-City, with main offices in Beijing, Shanghai, Berlin and Munich. The thesis here presented by Rodrigo Filipe Leite Rendeiro was executed as part of the department for Hardware Systems (LD DE HS) at the LiangDao office located in Munich, Germany. The scope of this thesis is a subset of the internal project "SiP LiDAR". This project is focused on development of Automotive LiDAR targeting integration on a b-pillar of vehicle with maturity of prototype. This project brings technological innovations in miniaturization, distributed system, sensor networks and digital signal processing that are required in future vehicles. The individual work was carried within a team of seven people in Munich and with support with remote colleagues located in Beijing, Shanghai and Shenzhen in China. As such, Rodrigo Filipe Leite Rendeiro, has interfaced with colleagues with different disciplines and cultural backgrounds. The thesis presents the individual achievements of Rodrigo Filipe Leite Rendeiro as part of the project work. As the project runs in a team-work environment, contributions from other members of the team are noted in the text where due. In addition, the individual contribution of Rodrigo Filipe Leite Rendeiro to the project and the company goes beyond what is presented in this thesis. Examples include support to other colleagues and department, contributions with expertise to hardware test and validation, as well as development of system architecture and technical discussions with external partners and suppliers. Moreover, Rodrigo Filipe Leite Rendeiro has acted as the local technical reference person for his subject and given a moderate level of autonomy and responsibility.

Palavras-chave

ADAS, LiDAR automotivo, lentes asféricas, FoV largo, sistema compacto, design óptico, polímeros óticos.

Resumo

Os sistemas avançados de assistência à condução (ADAS) permitem reduzir o número de acidentes rodoviários, melhorar a eficiência das indústrias de logística, e revolucionar o transporte urbano. De forma a desenvolver mais e melhores ADAS é necessário integrar o sistemas de deteção e medição de distâncias com luz (LiDAR) em veículos. Instalando sensores no pilar-b do veículo é possível obter dados da lateral do veículo. No entanto, para integrar o sensor no veículo é necessário minaturizar o LiDAR. Uma forma de reduzir o volume do sensor é usando óticas costumizadas, possibilitando a diminuição do tamanho das mesmas, que por norma ocupam o maior volume no sistema. Neste trabalho, de forma a diminuir o tamanho das óticas usou-se um design de óticas para smartphone aplicado ao LiDAR. Foram analisadas 3 soluções, sendo que se comparou o tamanho da média do quadrado da raíz do foco (RMS spot size), a função de transferência de modulação (MTF) e a distorção. Para avaliar a performance dos sistemas em operação, foi efetuado um estudo térmico para -25 °C, 25 °C, 60 °C e 125 °C para todas as soluções. Posteriormente, foi feita uma análise de tolerâncias, para avaliar os impactos na performance do sistema devido aos erros de fabricação inseridos.

Abstract   Advanced driving assitance systems (ADAS) allow to reduce the number of vehicle accidents in the road, increase the efficiency of the logistics industry and revolutionize the urban transport. To develop further and better ADAS functionalities there is a need to integrate light detection and ranging (LiDAR) sensors in the vehicles. To be able to integrate a LiDAR into a B-pillar to obtain data from the lateral of a car is necessary to miniaturize the LiDAR. One way to reduce the volume is decreasing the size of the optics, which usually occupies most volume, with custom optics. In this work, to decrease the stacking of the optics an optical smartphone design is applied to a LiDAR. Three solutions were analysed, with a root-mean-square (RMS) spot size, modulation transfer function (MTF) and distortion comparison. To evaluate the performance of the systems in operation, a thermal study for -25 °C, 25 °C, 60 °C and 125 °C was conducted for all the solutions. A tolerance analysis was also conducted, evaluating the variations in performance introduced by the manufacturing errors.

Contents

List of Figures

Acronyms

ADAS Advanced Driving Assistance Systems

ABS Anti-braking System

RADAR Radio Detection and Ranging

LiDAR Laser Detection and Ranging

SONAR Sound Navigation and Ranging

FoV Field of View

ECU Eletronic Control Unit

SNR Signal-to-noise Ratio

OEM Original Equipment Manufacturer

TOF Time-of-Flight

EEL Edge Emitting Laser

VCSEL Vertical-cavity Surface-emitting Laser

APD Avalanche Photodiode

SPAD Single Photon Avalanche Diode

FOI Field-of-Illumination

RMS Root-Mean-Square

MTF Module Transfer Function

PMMA poly(methyl methacrylate)

COC Cyclic olefin copolymer

COP Cyclo Olefin Polymer

PC Polycarbonate

CTE Coefficient of Thermal Expansion

CNC Computer Numerically Controlled

SPDT Single-Point Diamond Turning

TRAD tolerance on radius of curvature

TTHI tolerance on thickness

TEDX tolerance on element decentering in x

TEDY tolerance on element decentering in y

TETX tolerance on element tilting in x

TETY tolerance on element tilting in y

TIND tolerance on index of refraction

Chapter 1

Introduction

1.1 Motivation

According to the European Union, 95% of the accidents happen due to human error, with 22800 fatalities registered in 2019 [1]. One way of reducing the number of fatalities is to increase the adoption of Advanced Driving Assistance Systems (ADAS). ADAS use information of the vehicle surroundings gathered by sensors, complementing human senses, such as vision and hearing. They are composed of an array of systems that can alert and, in certain predetermined safety cases, can actuate to prevent accidents. These systems assist the user, while preventing for distractions, expanding human capabilities when operating vehicles [2, 3]. The ADAS can be traced up to the beginning of the 20th-century, with the introduction of a rudimentary mechanical cruise control system installed in a Wilson-Pilcher car [4]. The electronic cruise control was developed in late 1940s by Ralph Teetor and introduced in high end Chrysler Imperial models [4]. Anti-braking System (ABS), introduced in 1966 in Jensen FF car is another ADAS example [5]. Cruise control received an improvement in the 1990s with the introduction of adaptative cruise control and precrash systems, working as typical cruise control but using information obtained from sensors placed in front of the car, reacting and breaking in a needed situation [4, 6]. In the beginning of the 21st-century more systems were introduced in the market. Blind spot information (Radio Detection and Ranging (RADAR) information [7]), lane departure warning (using camera information [8]) and autonomous parking assistance systems (using ultrasonic sensors information [9]) were some of the systems introduced [10]. There are several sensors used to gather information for ADAS. In these it is possible to include moisture sensors, RADAR, ultrasonic sensors, cameras and LiDAR[11, 12]. Moisture sensors allow to detect the environment weather conditions the vehicle is facing (for example to detect rain). RADAR has been used for a long time in the naval and aeronautic industries, however, has poor object classification and edge detection [13]. Moreover, it has a low resolution due to the microwave frequencies allowed in the automotive area [11, 14]. Ultrasonic sensors (for example Sound Navigation and Ranging (SONAR)), are also used for a long time in the naval industry and work similarly as the RADAR, however, uses mechanical waves to sense. Since they use mechanical waves, they are affected by acoustic interference and changes in the medium, such as temperature and humidity, which affects the performance. When using the air as a propagating medium the detection range is very limited. These makes them usable for close range detection and at very low speeds, with application in parking assistance systems [11]. Another used mature

technology is camera sensing. However, is very sensitive to adverse atmospheric conditions or external lighting sources. Also, it is not possible to directly retrieve distance information. Thus, is necessary to combine the information with other sensors or, triangulating rays from multiple viewpoints with stereo cameras, mimicking the human eye perception vision [15].

LiDAR is an active 3D sensing emerging technology. It uses laser light to measure distances, with the transmitted wave reflecting in the object and being detected by photodetectors. It has a higher resolution than RADAR because the wavelength of the electromagnetic wave is several orders lower (nm order in LiDAR compared to mm order in RADAR). The most typical output of LiDAR is a point cloud, visible in Figure 1.1 (a)), recreating the 3D environment where the sensor is used [16]. One of the first practical applications of the LiDAR concept was to measure the distance from the Earth to the Moon. An experiment done in 1969, where the light took approximately 2.5 seconds to travel forward and back with an uncertainty of ± 25 cm [17]. LiDAR is already relevant at atmospheric particles or gases measurements [18], wind measurement to mitigate structural loads in the wind turbines [19] or geoscience ground measurements [20]. Its application in automotive industries had a global market value of 555 million USD in 2022 and is expected to grow to 3.10 billion USD by 2028 [21]. Table 1.1 compares sensing capability of several technologies with the human eye capabilities (since SONAR can only work for close range sensing is not considered in the table).

Table 1.1: Comparison of several sensing techniques and Human capabilities. Adapted from [13]

Performance aspect	Human	RADAR	LiDAR	Camera
Object detection	Good	Good	Good	Fair
Object classification	Good	Poor	Fair	Good
Distance estimation	Fair	Good	Good	Fair
Edge detection	Good	Poor	Good	Good
Visibility range	Good	Good	Fair	Fair
Poor weather performance	Fair	Good	Fair	Poor
Dark or low illumination performance	Poor	Good	Good	Fair

The RADAR and LiDAR can better detect objects, with LiDAR being able to classify the objects, due to a higher resolution [22]. This improves cameras information, especially in dark or low illumination situations, where cameras typically cannot retrieve reliable information. Usually, the presented technologies are merged in what is generally referred as sensor fusion [16]. With sensor fusion (see Figure 1.1 (b)) is possible to combine the advantages of each of the sensors. At the same time using multiple sensors allows to cover different failure modes, giving redundancy to the system [23]. This prevents the systems of creating the undesired situation of an unmanned vehicle generating accidents due to a malfunctioning sensor.

In order to develop further ADAS functionalities, namely autonomous driving in commercial vehicles, there is a need to integrate LiDAR in the vehicles, due to its ability to generate a high precision map of the surroundings [24]. Combining intelligent software with the sensor systems referred previously enables autonomous driving [25]. The implementation of autonomous vehicles in logistics allows to increase the efficiency in materials handling, inside factories and warehouses but also in trucks fleets [26, 27]. Autonomous vehicles can extend the fleets working hours and can help with the fleets parking. Another interesting point to note is the automation of public transports and unmanned taxi robots, increasing

the safety of all passengers while simultaneously increasing energy and time efficiency [27, 28].
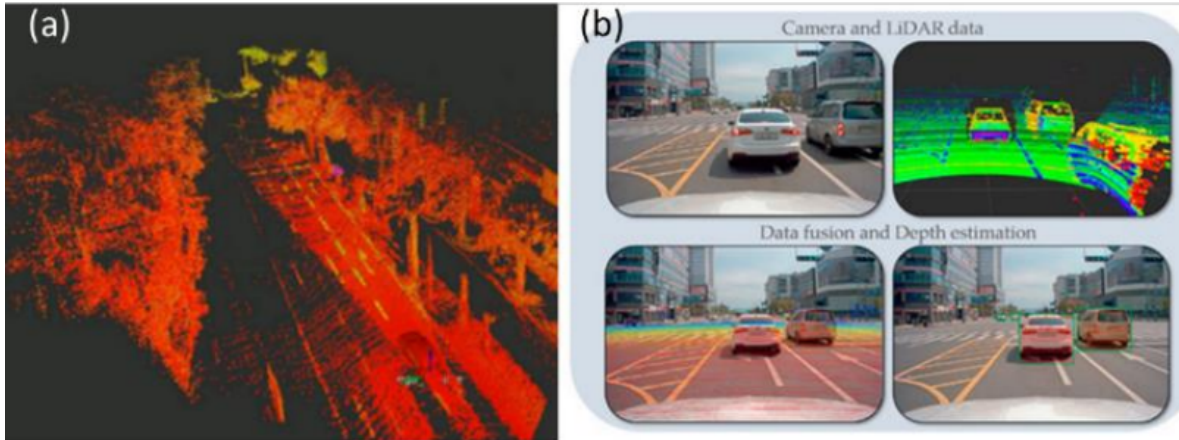
Figure 1.1: (a) Point cloud by IbeoNEXT LiDAR [29]. (b) Data fusion of LiDAR and camera [30].

One clear example is the test vehicles used for the development of autonomous driving functionalities of autonomous cars, in Figure 1.2. These examples serve as prototypes to collect real data. However, these prototypes do not have direct market application. This happens because they use a rotating LiDAR sensor on the top of the vehicle, covering a 360° FoV [31]. This solution beside affecting aesthetics, leads to increased noise, vibrations and drag, due to the sensors positioning [32].
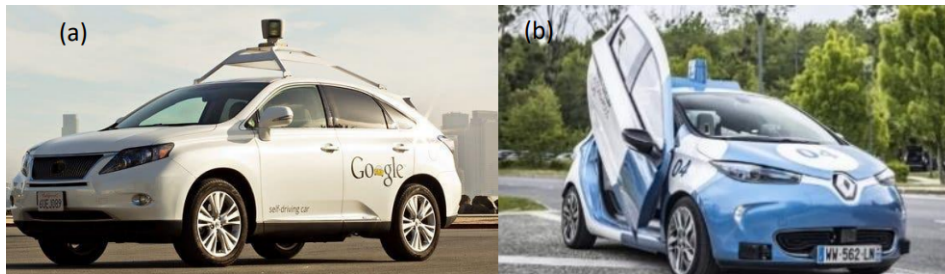
Figure 1.2: Example of test vehicles for development of autonomous driving functionalities using a rotating LiDAR system installed on top of the roof from (a) Google [33] and (b) Renault [34].

1.2 Problem statement

In this project, undertaken at LiangDao GmbH, instead of having a rotating LiDAR in the top of the car, the sensors are distributed and integrated around the vehicle. The already available automotive network is used to communicate between the LiDARs and the Eletronic Control Unit (ECU). The information is them combined, obtaining the surroundings information. This system is designed to be applied into the b-pillar of a car (see Figure 1.3). This application has requirements in FoV, volume of the sensor and temperature variations. The FoV requires to cover the lateral of the car. The volume needs to accommodate optics, housing, electronics and heatsink required for the sensor to work. Since the vehicles operate in several weather conditions the temperature also varies. The system is exposed to sunlight,

requiring wavelengths filters, cutting external undesired radiation, which degrades the Signal-to-noise Ratio (SNR)).
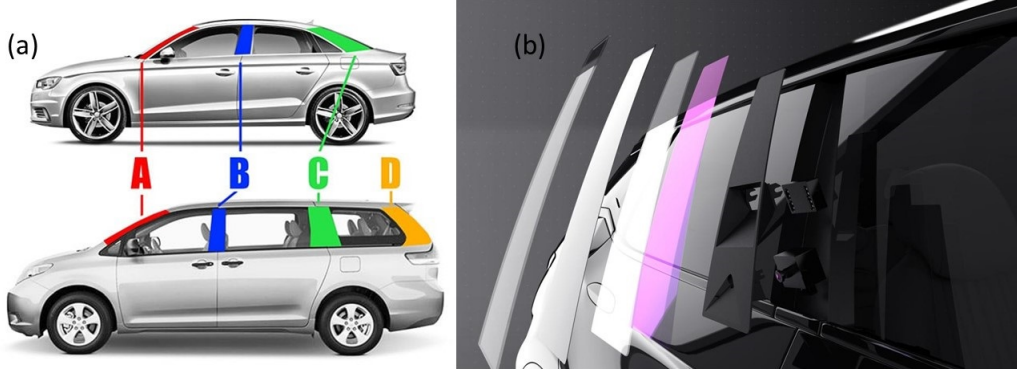
Figure 1.3: (a) Drawing exemplifying the pillars of a car [35]. (b)Exploded view of the sensor integration into the b-pillar of the car. The several layers represent the several coatings applied on the b-pillar by the manufacturer. The coatings act as protectors for UV radiation, protecting the parts from darkning due to sun exposure. They also filter the sun radiation being coated for transmiting 905 nm [36].

To be able to fit a LiDAR system in such a confined space, the typical main thickness contributor, the optics, need to be miniaturized while maintaining the FoV. Optics are an essential part of the sensor since they are passive elements, where with no energy use the overall efficiency of the system can be increased. The transmitter optics project the beams in the application required areas. The receptor optics collect and focus the photons of the laser beam onto the photodetector pixels [37]. The use of off-the-shelf components that could be easily bought in typical manufacturers, technically is possible. However, this approach leads to trade-off limitations that do not fit the requirements of the b-pillar integration. With off-the-shelf components is not possible to obtain the necessary FoV or the volume of the system for the b-pillar integration. The b-pillar has a certain thickness and curvature to be considered that affects real-life performance. Another limitation of this approach is the dependency on the pixel size and ratio of the detector. Also, the solution must be cost-effective especially when considering mass production, otherwise automotive Original Equipment Manufacturer (OEM) will not consider its integration into their products.

1.3   Objectives and thesis organization

The objective of this work is to design miniaturized imaging optics customized to be fitted in the receiver module of a LiDAR. The optics are optimized having in mind existing boundary conditions of a compact LiDAR with real application in the automotive market. Fitting the LiDAR with the custom optics allows to integrate the sensor in the b-pillar of the vehicles. Chapter 2 presents the principles of the used LiDAR systems and a overview of optics for a transmitter and for a receiver, with focus on aspherical lens manufactured in optical polymers. Chapter 3 discusses the optical design process and three solutions studied to achieve the goal of this thesis. Chapter 4 is focused on a thermal and tolerance analysis of the three designed systems, with a later summary on the analysis. Chapter 5 concludes the study in this thesis, while discussing some future work possibilities.

Chapter 2

Theoretical background and state of the art

2.1 LiDAR systems

There are different measurement principles for LiDARsystems, such as time of flight (TOF), amplitude or frequency modulated. The TOF corresponds to the time needed by the wave to be transmitted and received.

Defining the light pulse range as d, c as the speed of light and τ as TOF it is possible to define equation 2.1 [22, 38, 39]:

$$d = \frac{c\tau}{2} \tag{2.1}$$

Using c = 3 x 10^8 m/s, a distance (d) = 30 m gives a TOF of around 0.2 µs, which allows real time 3D sensing [22]. To create a point cloud of the environment is thus necessary to calculate individually each reflected beam.

For TOF there are two main approaches, scanning LiDAR, where the laser light is redirected using mechanical components or optical phased arrays and flash LiDAR, which diffuses a projected laser beam into a target scene. Flash TOF LiDARhas a more robust construction and it is a more cost-effective solution, because does not require movable parts, being also more close to commercial deployment [12, 16, 39, 40].

To achieve a compact solution is necessary to use semiconductor lasers. The options are EEL and Vertical-cavity Surface-emitting Laser (VCSEL). For VCSEL s, the light output is circular, while the EEL has an elliptical light output, visible in Figure 2.1.

EELs emit light parallel to the epitaxial structure, while VCSEL s emit light normal to the epitaxial structure. VCSEL s tend to be more cost-effective than EELs because all the manufactured lasers can be fabricated and tested prior to cutting the wafer [41]. This reduces assembly overall operation costs, driving the EEL price lower with the increase in manufacture.

However, the biggest difference is the outputted beam shape. Depending on the application, the elliptical beam requires optics to modulate one of the axis and round the beam, increasing overall costs and thickness of the sensor [41, 42].

Since the wavelength of the laser needs to be infrared the choice is reduced. Considering the near-infrared and shortwave-infrared wavelengths, the most commonly used wavelengths range from 800 to 1600 nm [12, 43]. The solar absorption spectrum has several minimums,

visible in Figure 2.2. Using these wavelengths allows to reduce the noise coming from sun radiation [12]. The 1550 nm is safer to the eyes than the others, and thus is possible to increase the range.
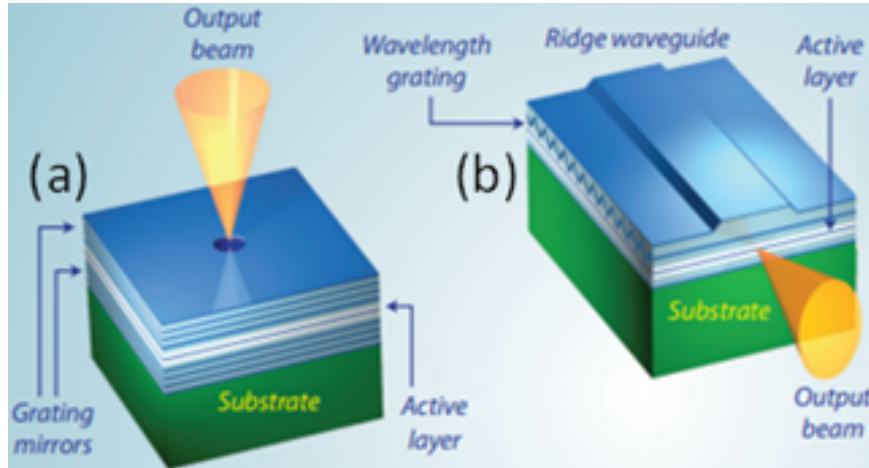
Figure 2.1: Output beam in (a) EEL (b) and EEL. Adapted from [41].
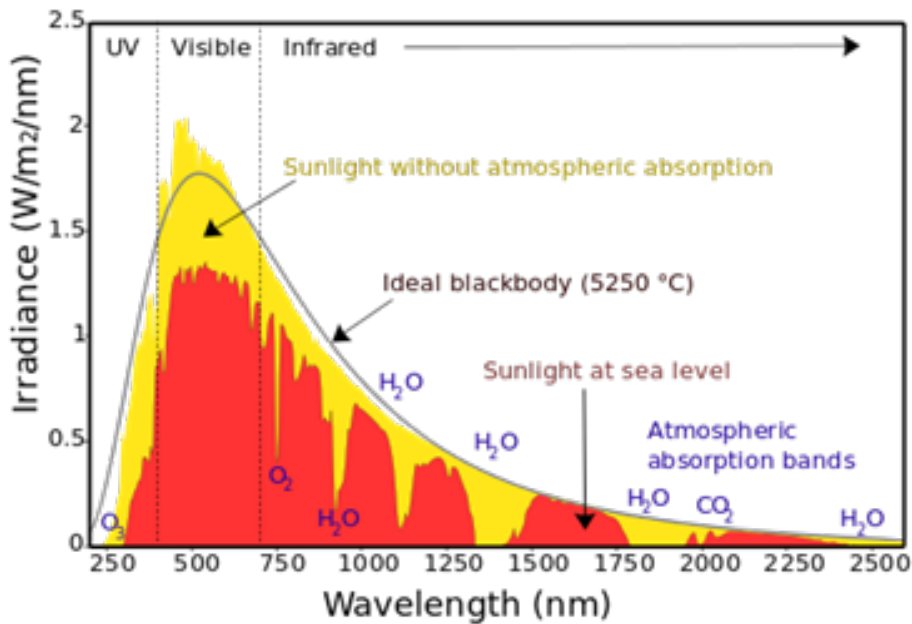
Figure 2.2: Earth spectrum of solar radiation, adapted from [44]

However, the fact that water molecules absorb this radiation better than the others makes this wavelength more prone to fail in adverse conditions (fog, rain, etc) [12, 45]. To note that the photodetector used, must match the laser wavelength and maintain a cost-effective solution [12]. In Figure 2.3 several materials for photodetectors responsivity dependence on wavelength are available. A negative point in using the 1550 nm wavelength is the higher priced photodetectors (which will detect the laser light). The 1550 nm photodetectors are made of InGaAs and Ge, a more expensive technology than silicon. Silicon is the cheapest

technology of these, due to its wide world availability and matured manufacturing industry
[12, 43, 46, 47].
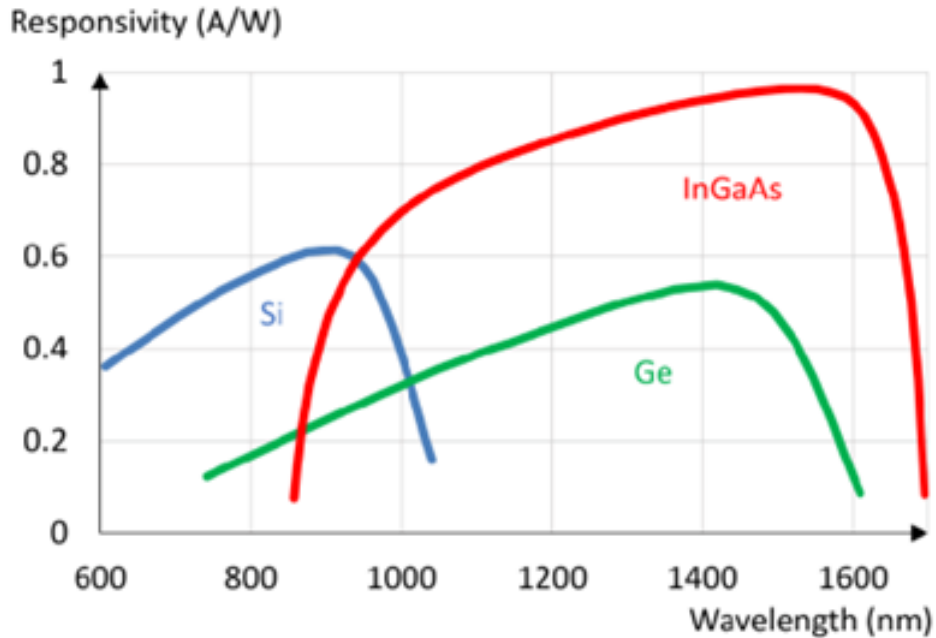
Figure 2.3: Silicon, InGaAs and Ge detector responsivity vs wavelength [48].

In the 800 to 1000 nm wavelength Si photodetectors as Avalanche Photodiode (APD) or
SPAD have a good responsivity. The responsivty decreases more than an order of magnitude
beyond 1000 nm when compared with the peak value [43]. Due to the stated, most of the
LiDARapproaches using pulsed TOF tend to use the 905 nm wavelength, attempting to
decrease the system price and size for the autonomous drive application.

The project at LiangDao is focused on a TOF flash LiDAR, using a EEL emitter at 905
nm and a silicon SPAD photodetector. The main modules are the laser, photodetector, lenses
and electronics (to control and process the signals), presented in Figure 2.4 block diagram.
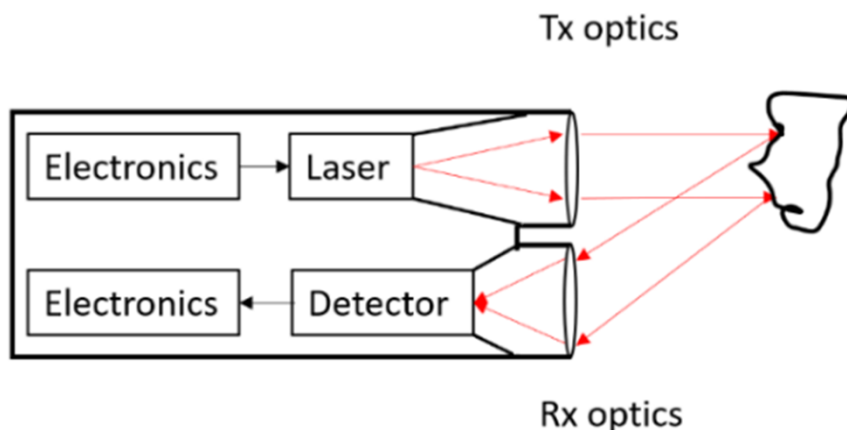
Figure 2.4: TOF LiDAR block structure.

The laser and its optics comprise the transmitter (Tx). The photodetector and its optics

comprise the receiver (Rx), which need to be synchronized in order to be able to distinguish the several pulses and corresponding TOF. In Table 2.1 it is available a comparison between some existing pulsed TOF LiDAR systems.

Table 2.1: Comparison of some of the available pulsed TOF LiDAR systems.

Available LiDAR	FoV (H x V) (°)	Angular resolution	Dimensions (mm)	Wavelength (nm)
Valeo SCALA Gen 2 [49]	133 x 10.5	0.125-0.25 x 0.6	137 x 191 x 123	905
SICK LD-MRS800001 [49]	110 x 6.4	0.125 x 0.8	165 x 93 x 88	905
MicroVision MOVIA [50]	60 x 37.5	0.23 x 0.38	108 x 103 x 83	905
Ouster DF0 [51]	130 x 65	0.33 x 0.16	120 x 110 x 70	850
ELMOS LiDAR cam [52]	60 x 25	0.25 x 0.3	40 x 30 x 35	940
ASC GSFL-16KS [38, 53]	60 x 60	0.47 x 0.47	22.1 x 82.6 x 197	1570
Hybrid LiDAR Systems Lissa [54]	80 x 33	0.33 x 0.42	70 x 35 x 70	905
LeddarTech Pixell [55]	177.5 x 16	2 x 1.9	245 x 86 x 130	905
XenoLiDAR Intercity [56]	60 x 30	0.3 x 0.3	170 x 110 x 80	905

Table 2.1 shows that the solutions in the market cannot be integrated in the b-pillar because they were not designed for that application. The higher FoV systems have dimensions much greater than the b-pillar. On the other hand, the system with the smallest dimension has a lower FoV, which would require more integrated sensors, raising the application costs.

2.2 Transmitter optics

The transmitter function is to project the laser power onto the scene intended to be illuminated. In order to be able to project it, the light generated by the EEL needs to be expanded from the small Field-of-Illumination (FOI) (the EEL divergence angle is around 20° [41, 42]) to the intended FOI . This can be accomplished by using a beam expander optical element. Diverging lens (see Figure 2.5 (a)), diffraction gratings (see Figure 2.5 (b)) or micro-lens arrays (see Figure 2.6) are examples of beam expander optics. The main requirement for the transmitter is that the FOI is smaller than the FoV, and the total track should match the receiver [57, 58, 59, 60].
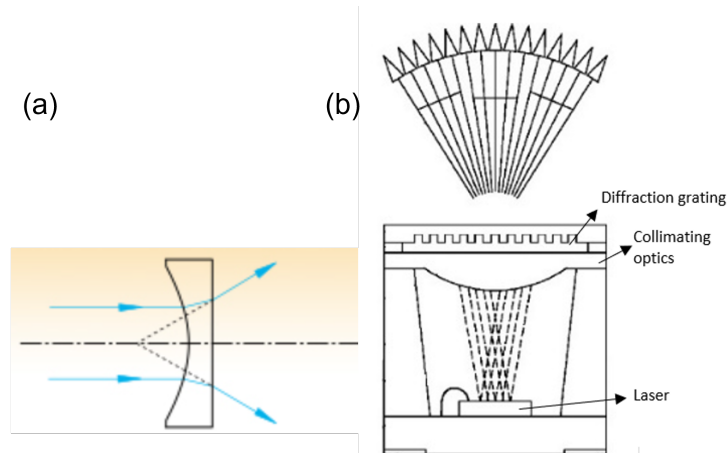
Figure 2.5: Beam expansion examples using (a) concave refractive lens [61] and (b) diffraction grating [62].

Using a refractive concave lens allows to increase the divergence angle, due to the high negative curvature radius [57]. With diffraction gratings instead of using the material refractive power, the increased angle is due to diffraction of the light in the grating slits, but usually requires a pre collimated beam [58, 62, 63].
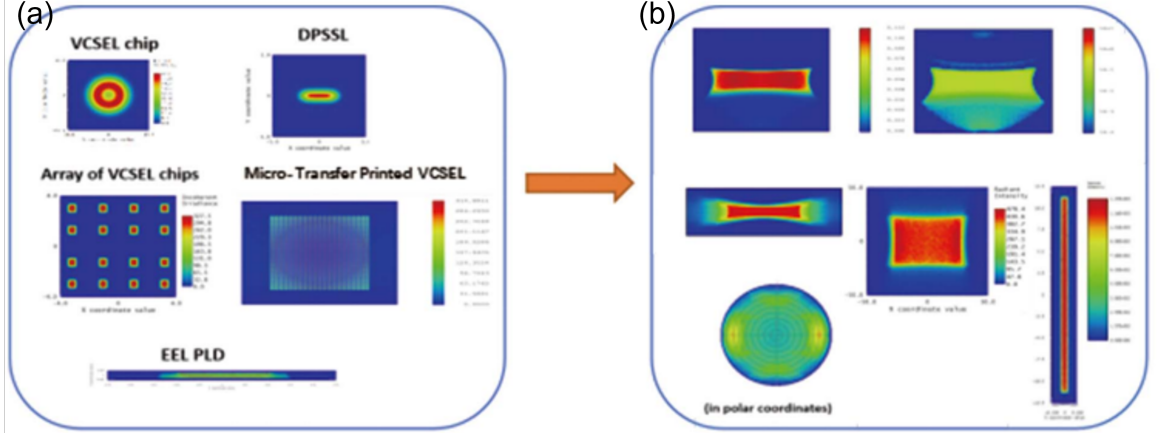
Figure 2.6: EEL beam expanding using micro-lens array. (a) Before micro-lens array. (b) After micro-lens array. Adapted from [59].

The micro-lens array made of a high refractive index material, allows to decrease the volume of the optics, when compared to classical concave lens. Also, when dealing with an array of sources, for instance a EEL array, is preferable to use micro-lens array to better diffuse the light, again compared with classical concave lens. Also, to decrease losses in transmission it should use the minimum elements possible [59, 64, 60].

2.3   Receiver optics

The receiver is constituted by a photodetector and imaging optics. The function of the imaging optics is to collect the laser signal reflected by the target and focusing it on the photodetector. The purpose of imaging optics is to resolve a predetermined minimum size object over the desired FoV [65]. It is possible to use refractive or diffractive optics in an imaging system. Despite diffractive optics allowing a higher miniaturization of the system, the higher costs turn them inviable to apply in the project.

2.3.1   Description of a refractive optical system

Bellow is a list of the key concepts for refractive optics, and ways to evaluate its performance in image quality. Later, a brief description of the typical systems, its key components, materials, manufacture and assembly methods and tolerances will be made. In Figure 2.7 a diagram with common first-order representation of a generic optical system is available with a representation of the marginal and chief ray, the optical axis and focal length. In Figure 2.8 is a single lens drawing with some concepts explained.

- Paraxial focus represents the point where the rays entering perpendicular (or almost perpendicular, if the angle between the perpendicular and the ray is ≈ to the sin of the angle can be considered in the paraxial regime) to the lens plane converge [66].

- Aperture stop, "[...] the surface in the system where all of the chief rays from different points in the object cross the optical axis and appear to pivot about." [65].

- Curvature sag is the height measured in the z axis (considering a cartesian referential, with z as the optical axis, and xy the lens area) in function of x and y [65, 67].
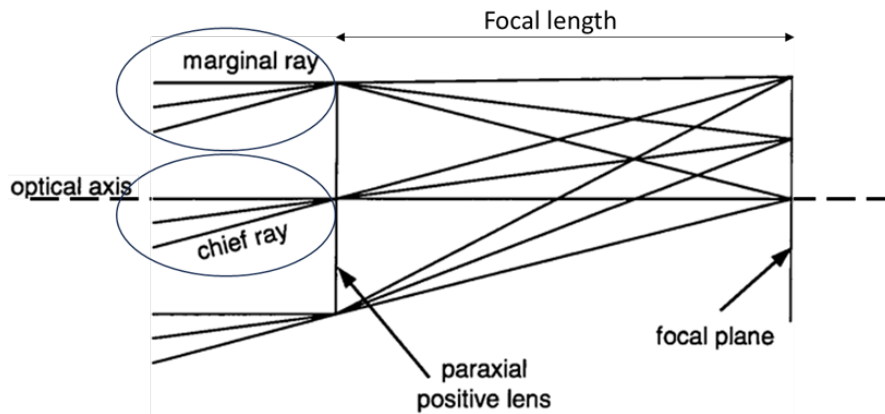
Figure 2.7: Representation of a paraxial positive lens and marginal and chief rays. Adapted from [65].
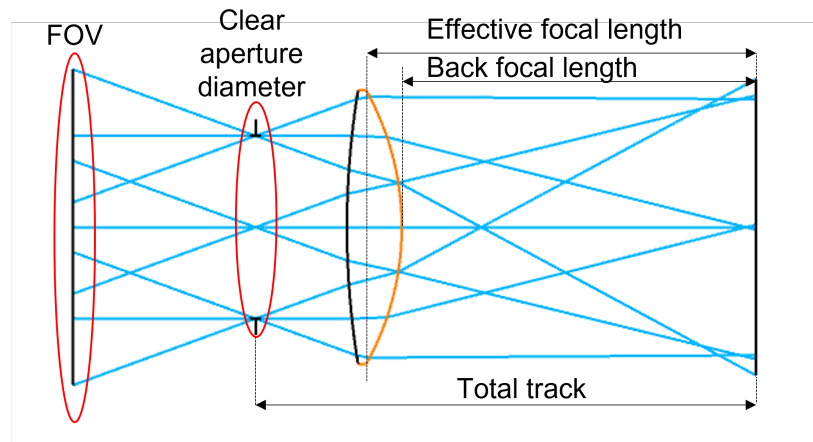
Figure 2.8: Drawing of a single lens system legended with some key concepts.

- The Fnumber (F#) defines "the final imaging cone reaching the image at its centre[...]" [65], calculated using Equation 2.2. For a fixed effective focal length (efl), a smaller F# lens system will collect more light.

$$Fnumber \ (F\#) = \frac{Effective \ focal \ length}{Clear \ aperture \ diameter} \tag{2.2}$$

- The refractive index (n) represents the ratio between the velocity of the wave in vacuum and in a certain material. Represents the capacity of refracting a ray of a certain material [66], and is directly proportional to the optical power.

2.3.2 Image quality indicators: aberrations and diffraction

The Maxwell criteria for perfect imaging states that all rays that emerge from an object point converge to a single image point. "Aberrations are the deviations from perfection of the optical system" [68]. There are several geometrical aberrations some of them being chromatic and some monochromatic, extendedly explained in [66]. Since the system uses monochromatic light only the second ones will be referred.

Spherical aberration: is the distance between the axial intersection of the paraxial focus and the marginal ray entering parallel to the paraxial focus (see Figure 2.9). If discussing a converging lens, it will be positive, and in the diverging case since it will intersect the axis behind the paraxial focus, will be negative [66].
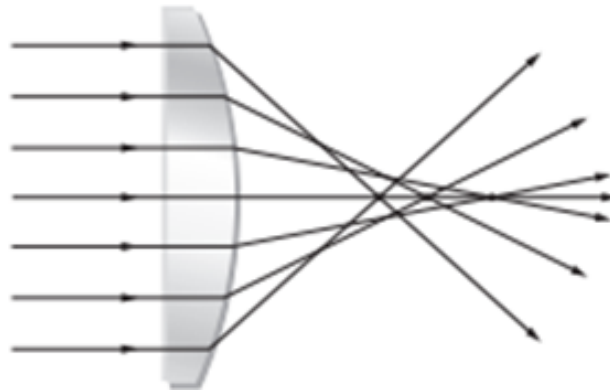
Figure 2.9: Spherical aberration caused by a planar-convex lens. Adapted from [66].

Coma aberration: The transverse magnification will differ from rays propagating off-axis regions of the lens because its effective focal length will differ. If the image point is off-axis and the incident rays are oblique, coma will be evident, as visible in Figure 2.10. Usually, this aberration will create a blur similar to a comet trail [66].
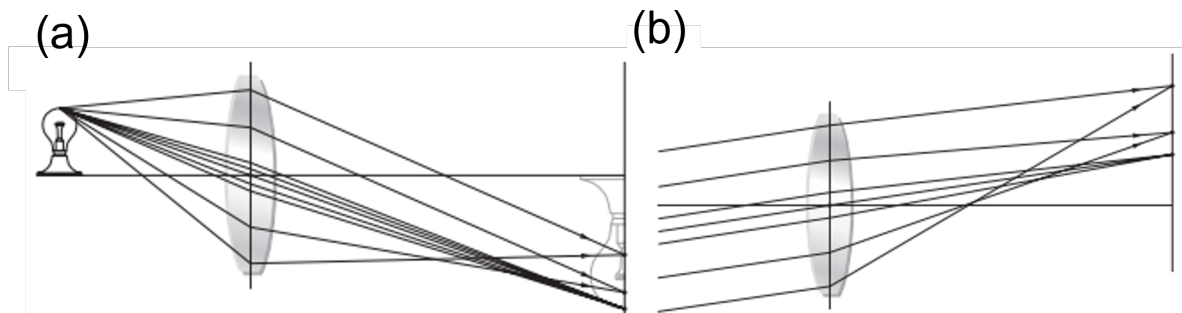
Figure 2.10: (a) Negative coma and (b) positive coma. Adapted from [65].

Astigmatism: If the object points to be imaged lie in an appreciable distance from the optical axis, the cone of rays will hit the lens asymmetrically. Looking at the trajectory of the rays in 3D, what will happen is that the chief ray from the sagittal plane and the tangential plane will have different focal lengths, visible in Figure 2.11. This happens because the tangential rays (the rays in the tangential plane) are tilted with more respect to the lens,

having a shorter focal length. Astigmatism will increase as the object point moves farther off-axis and does not exist on paraxial regime [66].
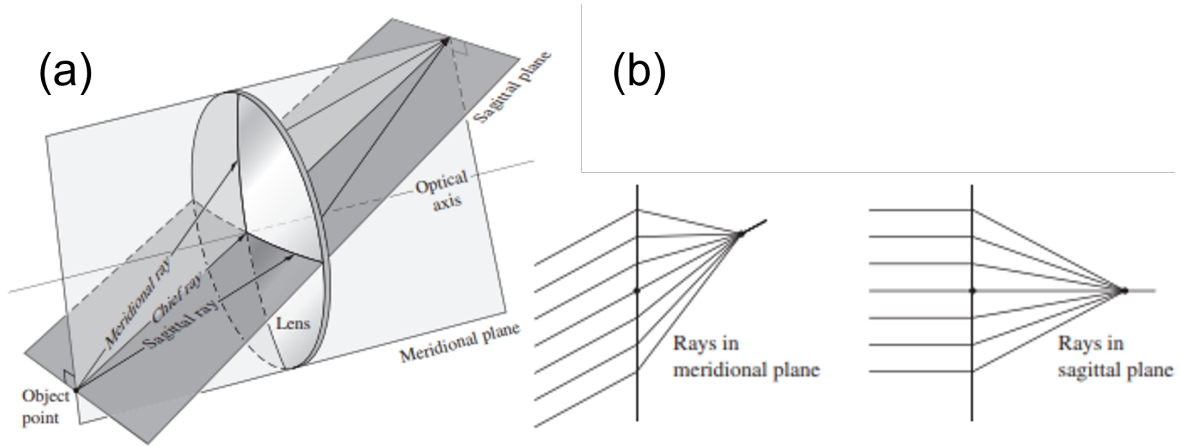
Figure 2.11: (a) Tangential/Meridional and sagittal planes and (b) Focal length in the different planes. Adapted from [65].

Petzval field curvature: the object and the image at the same distance as the centre of a lens are displaced in a circumference, considering both the object and the image a plane. The focal distance for objects off-axis will be different from the ones on-axis, resulting the Petzval Field Curvature aberration, as can be noticed in Figure 2.12 [66].
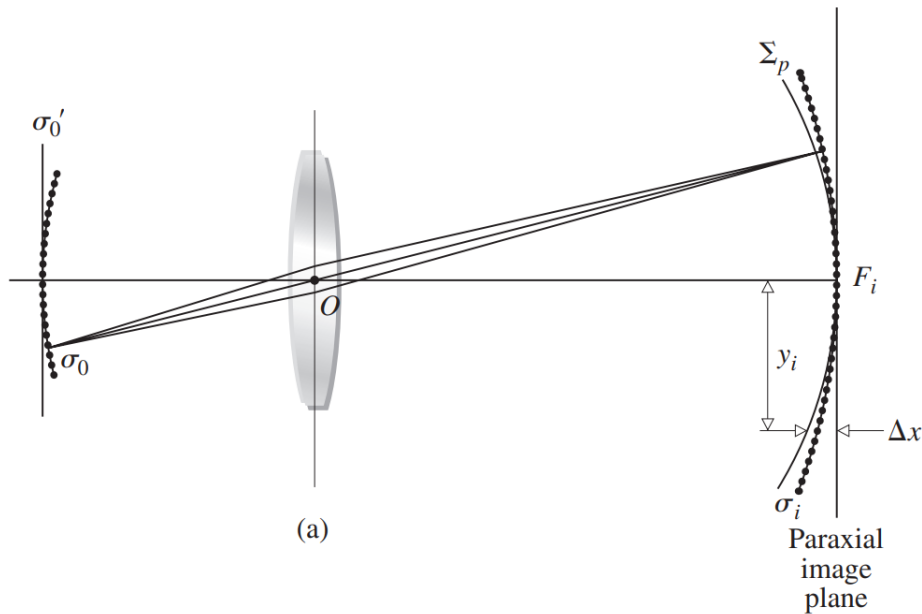
Figure 2.12: Diagram representing Field Curvature aberration, with the highlighted difference in the image plane and focusing plane. Adapted from [66].

Distortion: it happens because different areas of the lens have different focal lengths, and due to that have different magnifications. What will happen is that the image will have different magnifications radially around the centre of the lens. The distortion can be positive,

and expand the corners of the image (pincushion distortion), due to a higher magnification off-axis. It can also be negative, contracting the edges of the image (barrel distortion), related to a higher magnification on-axis [66], visible in Figure 2.13.

(a)   (b)   (c)
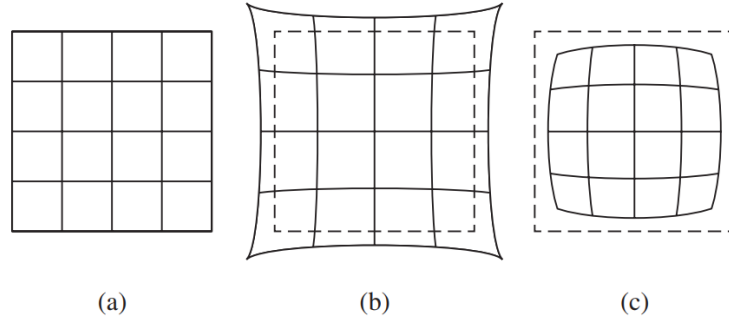
Figure 2.13: (a) Undistorted image. (b) Pincushion distortion. (c) Barrel distortion. Adapted from [66].

Table 2.2 summarizes the reviewed aberrations dependence on aperture and incidence angle, allowing to easily understand the aberrations behavior.

Table 2.2: Summary of reviewed aberrations dependence on aperture and incidence angle. Adapted from [65].

Aberration	Aperture	Incidence angle
Spherical	Cubic	n.a.
Coma	Quadratic	Linear
Astigmatism	Linear	Quadratic
Field curvature	Linear	Quadratic
Distortion	n.a.	Cubic

If the geometrical aberrations are corrected the system will still face a diffraction limitation. The diffraction is caused due to the light interacting with the limiting edge of an optical system, creating a disk (due to circular symmetry) with a profile of a "small gaussian intensity function surrounded by low-intensity rings of energy" (see Figure 2.14) [65].
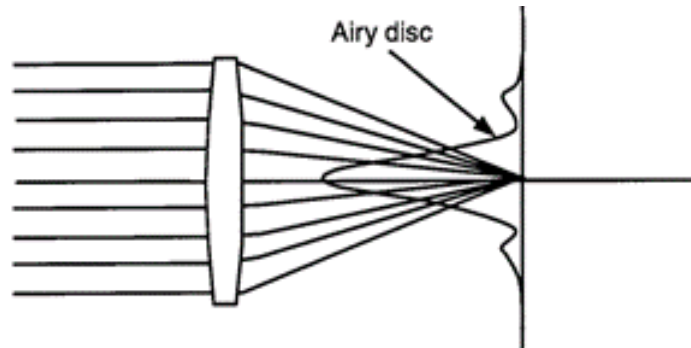
Figure 2.14: A diffraction limited lens and the corresponding airy disk. Adapted from [65].

The airy disk radius represents the ideal theorical angular resolution of a perfect imaging

13

instrument [66]. The diffraction limit angular resolution can be calculated using Equation 2.3

$$Angular\ diameter\ of\ Airy\ disk = \frac{2.44\lambda}{Clear\ aperture\ diameter} = Object\ space\ angle \quad (2.3)$$

If the geometrical aberrations cannot be corrected and are bigger than the diffraction limit of the system, they will dominate the image formed. In this case, the angular resolution can be calculated using Equation 2.4:

$$Angular\ resolution = Object\ space\ angle\ = 2tan^{-1}(\frac{object\ size}{2 distance\ to\ object}) \quad (2.4)$$

The angular resolution can them be used to calculate the spacial resolution using trigonometry and the distance to the object, as in Equation 2.5

$$Spatial\ resolution = sin(Angular\ resolution) distance\ to\ object \quad (2.5)$$

2.3.3 Performance evaluation of the system

There are several performance indicators for an optical system. The ones considered more relevant for an imaging system are:

RMS spot size diagram: measures the diameter that encircles around 68% of the energy imaged from a point source (see Figure 2.15). They are useful in systems with pixelated detectors, giving a measure of the radius where the object is going to be imaged. It is also possible to retrieve information about the aberrations present in the system [65].
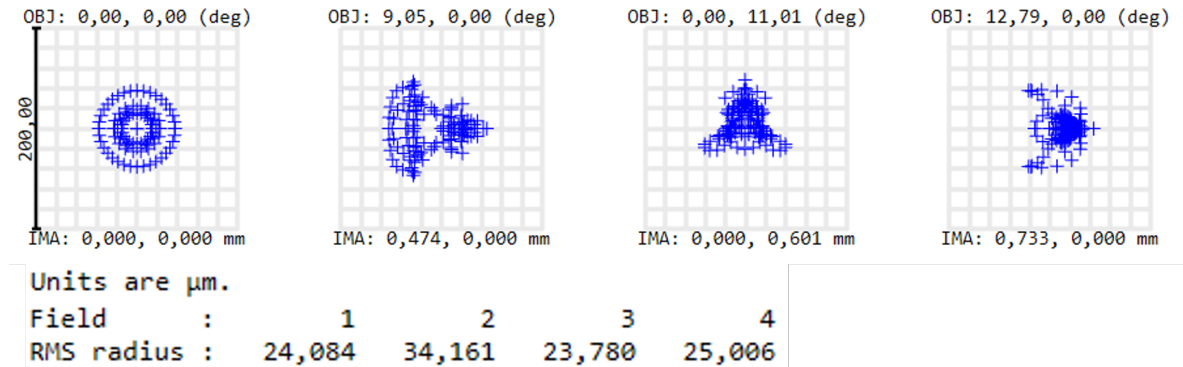
Figure 2.15: Example of a spot size diagram with RMS values for different FoV.

MTF: represents the ratio of the modulation in the image to the modulation in the object as a function of spatial frequency (see Figure 2.16). In other words, MTF gives a value in percentage of the observable contrast between the maximum and minimum intensity (usually in function of the number of line pairs per millimeter of the test image) [65]. MTF value should be as close as possible to the diffraction limit. However, in applications with several constrains is not always possible to have such a higher MTF. According to [69] if the values presented in Table 2.3 are meet good imaging quality can be obtained. All these values are for half of the Nyquist frequency, and are represented in line pair/mm which is the typical unit to measure the MTF. Can be calculated using Equation 2.6:

$$Sensor\ resolution\ (linepair/mm) = \frac{1\ line\ pair}{2\ pixel\ size} \frac{1000\ \mu m}{1\ mm} \quad (2.6)$$
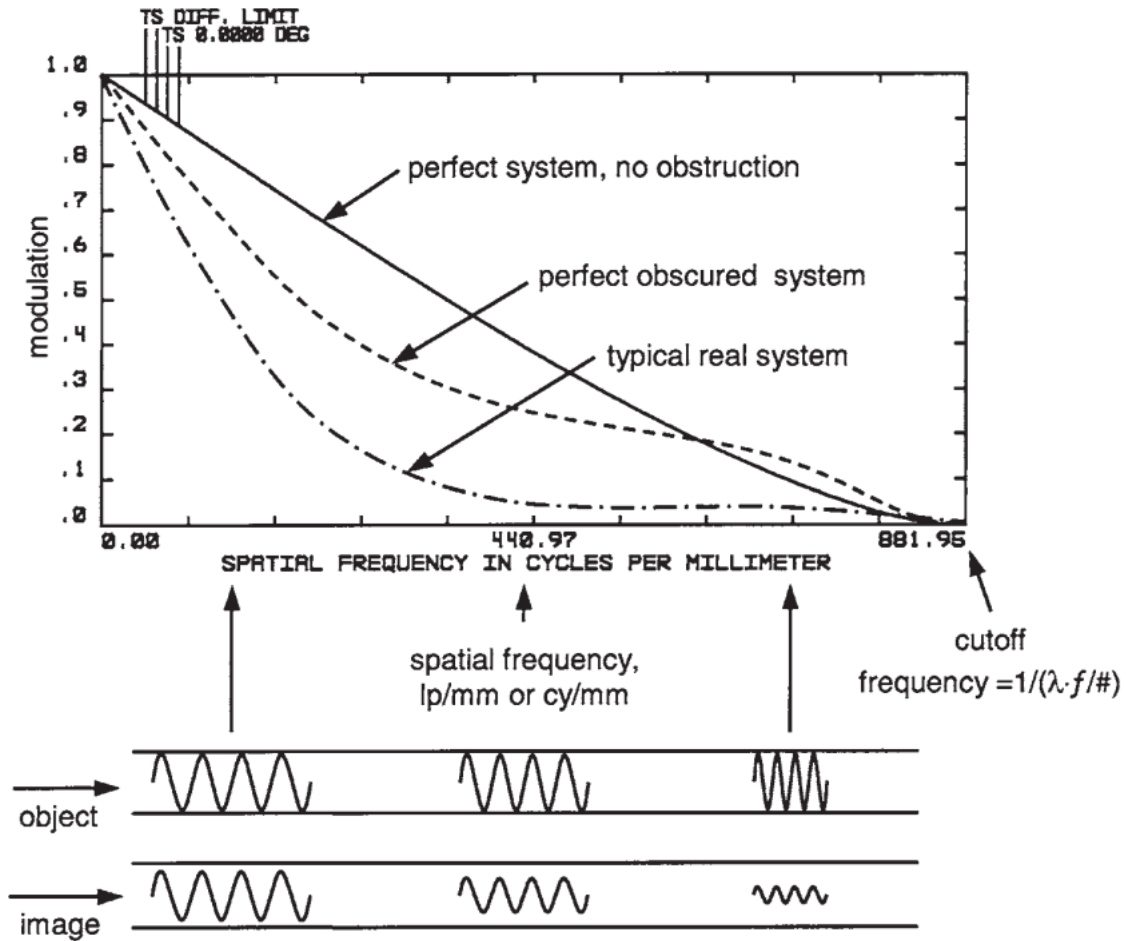
Figure 2.16: Typical MTF Curves for imaging systems [65].

Table 2.3: MTF values (for sagittal/tangential planes) at half of the Nyquist frequency of the sensor for good imaging quality.

MTF	On-axis (0° FoV)	70% off-axis (70° FoV)	100 off-axis (100° FoV)
sagittal plane	60%	50%	20%
tangential plane	60%	40%	10%

2.3.4 Typical wide FoV lens systems

The retrofocus lens design is a classical wide FoV lens system. Usually is composed by two different groups separated by a large airspace (see Figure 2.17). The first group (from left to right) typically is a negative power group (negative focal length), reducing the incident angles and the second one is a positive group, focusing the rays into the image plane

Commonly, they have a greater back focal length compared to its effective focal length. To note that this kind of designs have large diameter lens and total track. Wide FoV retrofocus design systems suffer from significant negative distortion, creating a noticeable barrel distortion. Usually, this distortion is difficult to correct, being usually balanced with a higher order positive distortion.

15

The cemented lens (the lenses glued together), made of different materials, are there to correct the chromatic aberrations, not stated on chapter 2.3.2 because as it was referred, the system in this thesis uses monochromatic laser light [70].
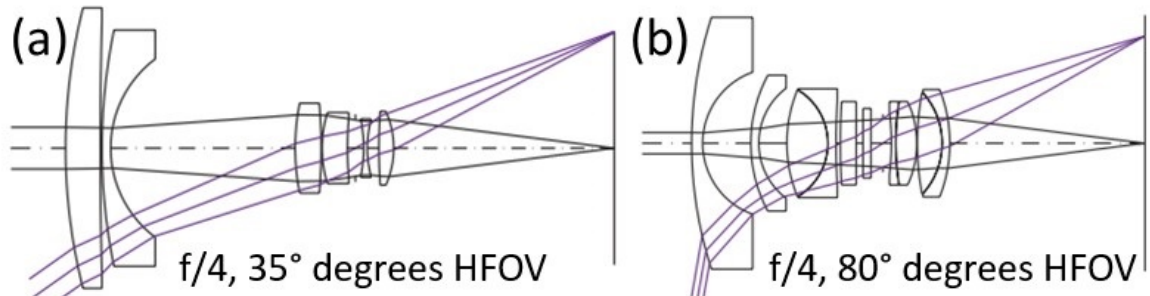
Figure 2.17: Retrofocus wide angle designs with an F# = 4 and a FoV of (a) 70° and (b) 160° [70].

One well known variation of the retrofocus is the Fisheye, usually achieving a 180° FoV, but suffering from a severe negative distortion [70]. Figure 2.18 is a drawing from a Nikon Corp patent for a Fisheye lens system with 180° FoV, F# = 2.8 and the total track = 101.9 mm.
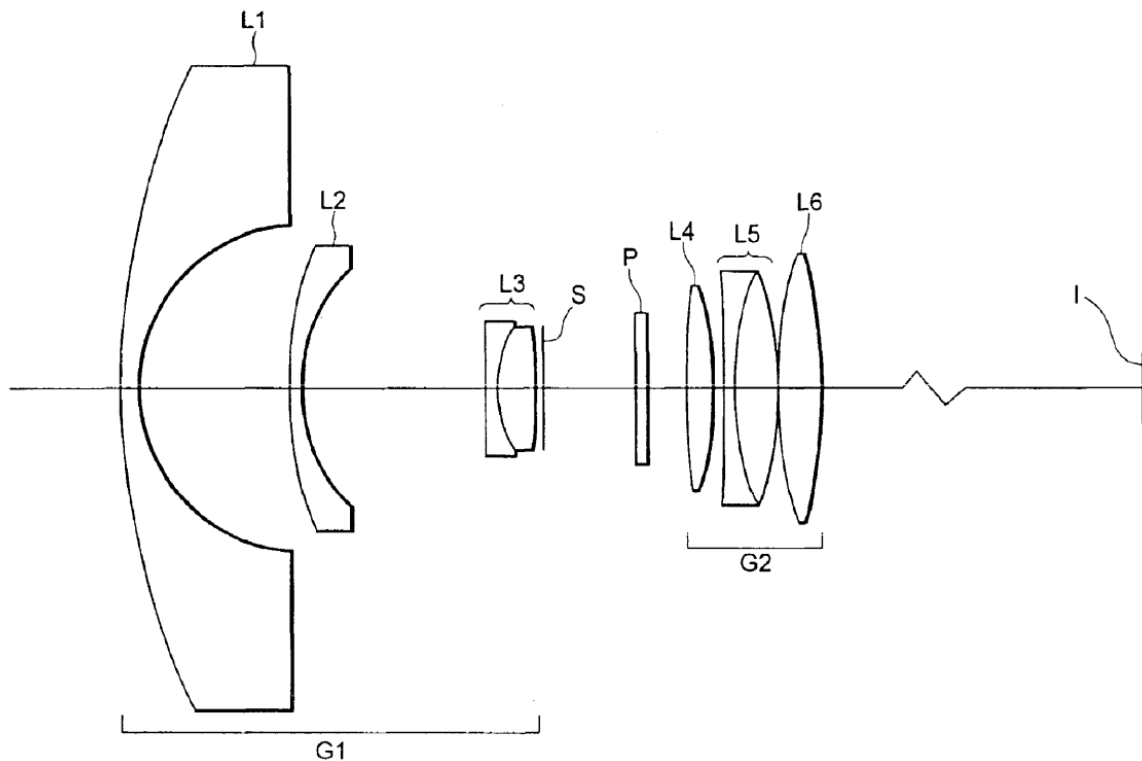
Figure 2.18: Optical system from patent US6844991B2 for a 180° FoV Fisheye lens. The focal length of the system is 10 mm, with a F# = 2.8 and a total track = 101.9 mm [71].

Fisheye systems, as a typical retrofocus design has two lens groups, with the first one having a negative power group (lens L1 and L2) and the second one a positive power group.

The main difference to the designs in Figure 2.17 is the first lens, a meniscus lens.

The meniscus lens has the same curvature on both sizes, allowing to collect light with a wider angle of incidence with the same focal length. However, the trade-off of using the wide diameter meniscus lens in the front is the increase in distortion. The stop is usually located at the center of refractive power, using symmetry to help balance the aberrations such as distortion, coma and astigmatism [65].

The second group has cemented lens to correct for chromatic aberrations [71]. These systems can achieve a high FoV with a relatively small F#, however they have a very long total track that would make the sensor integration in a b-pillar unfeasible.

In the last 20 years imaging systems suffered a major optimization towards miniaturization, especially with the advent of smartphones cameras, who pushed the limits of miniature imaging. The system presented in Figure 2.19 (a) comprises 7 lenses, the first lens (from left to right) has a positive power, to help reduce the total track. In Figure 2.19 (b) a smartphone camera cross-section compared to a coin highlights the compactness of such devices. Despite being very miniaturized (usually the thickness is less than 1 cm, which needs to account for the housing and electronics), smartphone lens systems are still able to produce high resolution images. Another advantage to refer is their ability to also achieve a wide FoV (been able to reach 100°) [72, 73, 74]. The last 3 lenses are highly aspherical, decreasing the number of elements in the system, while correcting the aberrations present in the system, consequently reducing the total track of the system [74, 75, 76].
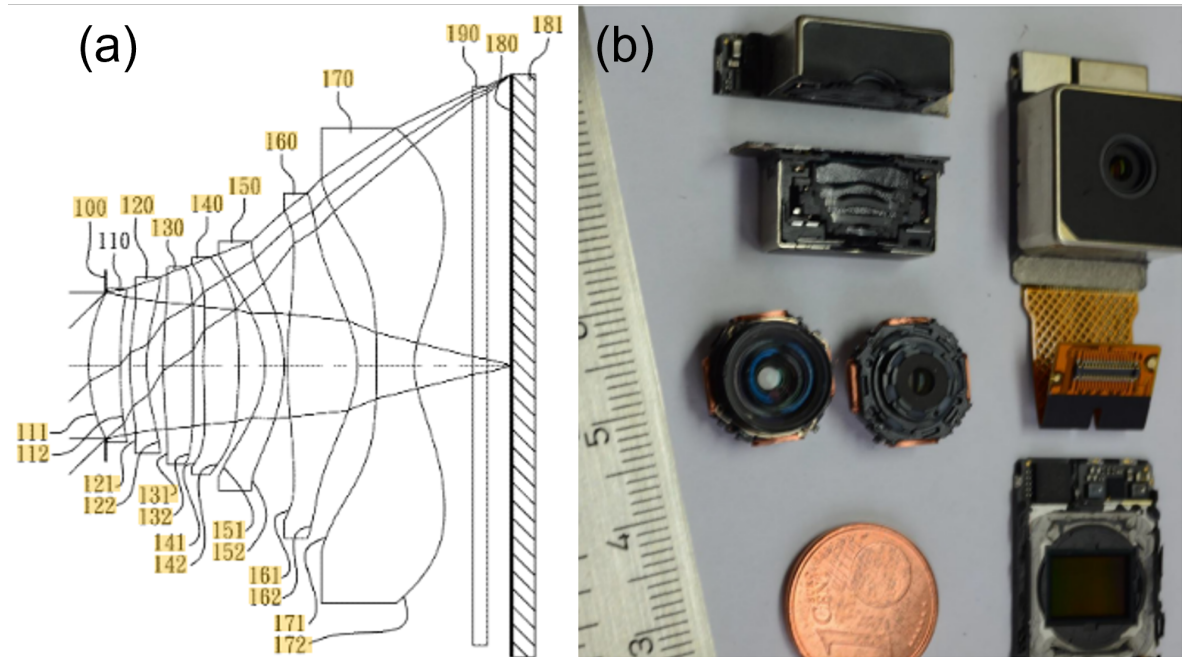
Figure 2.19: (a) A smartphone wide angle patent drawing [74] and (b) a smartphone camera module compared to a 1 cent coin [72].

To note that the aperture stop is located before the first lens to improve the image-sensing efficiency on the photodetector. This system has a FoV of 88.6 °, F# = 2.00 with a total track = 5.8 mm [74]. The high FoV combined with the small total track makes them the best candidate designs to fit into a miniaturized LiDAR.

17

Aspheric lenses

The aspheric lenses are lenses in which the surface profile is more complex because it has inflection points, diverging them from the typical spherical shape. If they are close to the aperture stop, they will mainly correct the spherical aberration, but if they are closer to the image plane, they can correct other aberrations in the system [65], visible in Figure 2.20.
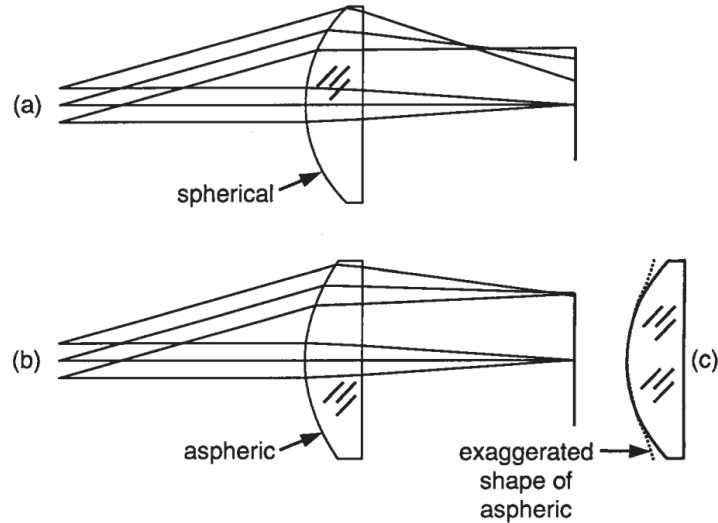
Figure 2.20: Astigmatism correction comparison between spherical (a) and aspherical (b) lenses. (c) Surface shape comparison [65].

The deviation from sphere form makes their manufacturability more complicated (due to the variations in the surface), but as referred before, they allow to improve the total track and reduce the aberrations present in the system, allowing also to reduce the number of elements in the system. There are a lot of different shapes for aspheric surfaces, having different equations defining it. In Figure 2.21 is possible to observe the variation in the lens form for several order coefficients.
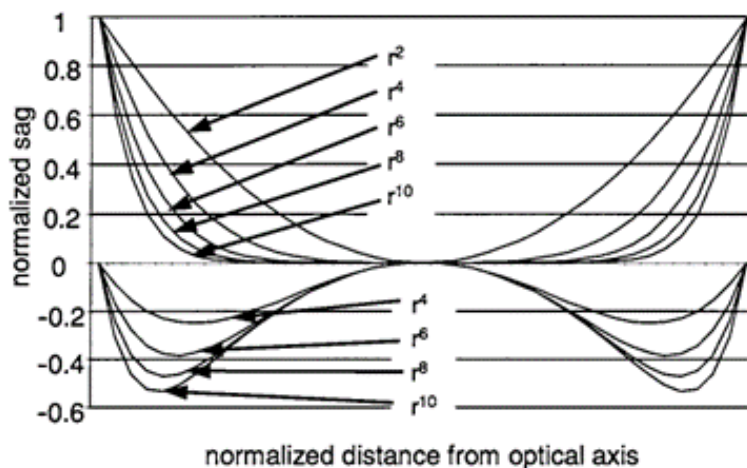
Figure 2.21: Aspheric Sags due to different coefficients. Adapted from [65].

For a rotationally symmetric surface, the curvature sag of the surface (z) is defined by

Equation 2.7:

$$z = \frac{cr^2}{1 + \sqrt{1 - (1+k)c^2 r^2}} + \sum_{n=1}^{N} a_i r^2 i \qquad (2.7)$$

With c as the vertex base curvature, k the conic constant, r is the radial coordinate measured perpendicularly from the optical axis, and the sum corresponding to higher order aspheric terms [65, 67].

2.3.5 Materials, manufacture, tolerances and mounting for aspheric lenses

To decrease the costs of manufacturing, the lens can be produced in optical polymers. Polymer materials allow to have more complex geometries than glass, being able to easily mass manufacture components with diameter of a few millimetres. In Table 2.4 several properties of optical glass,PMMA, Cyclic olefin copolymer (COC), Cyclo Olefin Polymer (COP) and Polycarbonate (PC).

Table 2.4: Possible materials to fabricate aspheric lens. Adapted from [77].

Material type	PMMA	COC	COP	PC	Glass
Refractive index (905 nm)	1.4832	1.5037	—	1.5672	1.5089
Density (g/cm^3)	1.19	1.02	1.01	1.20	2.51
CTE (x10^{-6})	67	60-70	60-70	66-70	7.1
dn/dT (x10^{-5})	-8.5	-10	-8	-12 to -14	3
Water absorption (%)	0.3	0.01	<0.01	0.1	0.1
Relative cost	Low	Medium	High	Medium	High

Optical polymers also exhibit better moldability than glass, making them better suitable for mass production methods using a replicating molding process, reducing even more the unit cost of the lenses. In counterpart, polymers have a higher sensitivity to changes in temperature, in terms of the volume, Coefficient of Thermal Expansion (CTE), and optical power (refractive index variation (dn/dT)).

The spectral range of these materials is lower when compared to glass, being above 90% in the range of 450-950 nm for the most optical polymers [77]. Optical glass such as N-BK7 from Schott achieve a transmission above 90% in the range of 350-1600 nm. Optical polymers allow to reduce the cost of the system, being its value at least ten times lower than its glass equivalent using traditional methods like grinding and polishing, which reduces prototyping costs. The density of optical polymers is lower than glass, allowing for a weight reduction.

The coating of polymers is formed at lower temperatures than the temperatures used for glass, resulting in generally less dense layers. There is also a higher difficulty in achieve a proper adherence of the coating to the surface and the coating can crack during the process. This can happen, for example, due to mechanical growth stress of the coating or thermal mismatch between the coating and the substrate, when the system is heated for film deposition (and cooling after deposition).

Nevertheless, is possible to apply anti-reflection coatings on the surface of the lenses, being easier to coat COC than PMMA). The coatings overall increase the transmitted light and avoid the formation of ghost images in imaging systems [78], improving the imaging quality.

The standard techniques used for prototyping (and medium volume production) are Computer Numerically Controlled (CNC) and Single-Point Diamond Turning (SPDT). CNC

and SPDT are techniques in which the materials are grinded and polished with computer automated tools. The main difference between the two is that SPDT uses a diamond-tipped tool to carve the geometry into the polymer, allowing to have a nanometer-level accuracy.

Polymers can be ultrasonically cleaned to remove imperfections in the surface when using SPDT. It is also possible to use CNC to reduce the SPDT time, using the last just to remove the material needed for the precision. Usually, these polymers require a stress relaxation cycle, with annealing. This step reduces the cycle time required for the SPDT, which is the higher cost in manufacturing [77]. Table 2.5 presents some tolerances for SPDT optical plastics.

Table 2.5: Typical SPDT manufacturing tolerances for aspherical lenses. Adapted from [77].

Specification	Lower-Cost Tolerances	State-of-the-Art Tolerances
Radius of Curvature	±1-2%	±0.15-1.00%
Surface roughness	100 Å	60 Å
Centration/Runout	±0.025 mm	±0.005 mm
Thickness	±0.025 mm	±0.005 mm
Diameter	±0.050 mm	±0.005 mm
Part-to-Part repeatability	$0.5 - 1.0\%$	$0.03 - 0.05\%$

For mass production, the usual method is injection molding. This method consists of injecting the liquified chosen polymer into a mold. In the process the main cost driver is the mold. However since it can be reused this allows to reduce the unit cost for mass-production, as well as the lead time, when compared to the other methods referred. The parts are produced in a cleanroom environment, but there is a need to remove the gate vestige (from the mold). To remove it they can go through a process of automated laser degating without leaving the clean environment. This eliminates the unit-to-unit variability and human impacts on hand cleaning the parts. Laser degating is a technology in where the laser power smooths the surface of the lens around the gate vestige [77].

Optical polymers also have the advantage of easily manufacturing alignment and mounting features, which decreases the complexity of mounting multi element optics systems. This also helps to decrease the mounting costs and improve the systems consistency. To mount the lens and align them, the process uses the same techniques used for glass materials. The most common ones are "drop-in" for lower tolerances and active alignment for a higher precision. In Table 2.6 is possible to observe assembly tolerances for actively aligned polymer optics.

Table 2.6: Typical tolerance values for actively aligned polymer optics [77].

Specification	Lower-Cost Tolerances	State-of-the-Art Tolerances
Axial position	±10 µm	±1 µm
Tilt	±6 arcsec	±1 arcsec
Decentration	±10 µm	±0.5 µm

"Drop-in" consists of dropping the lens in mechanical holders, using the gravity and the surface constraints to fit the optics in the system. The active alignement uses a laser source to attest the tilting and decentration of the component. A spin chuck or piezo-electric components can them be used to correct the alignment. Both the processes finish with a mechanical bonding agent cured using ultraviolet or heat. The bonding agent refractive index should match the polymer refractive index, to minimize reflectance between the components surfaces [77].

Chapter 3

Optical components design

3.1 Boundary conditions

In chapter 1 it was referred that the b-pillar integration of the LiDAR introduces constraints to the system. These constraints must be considered when designing the system, otherwise, when integrating, the performance will be reduced. The b-pillar in Figure 3.1 was used in the development of the optical design, where the PMMA optical window to integrate has 55 mm width, 45 mm length, 3 mm thickness and a curvature of 1440 mm. For the integration there are 30 mm available, which need to be shared by the housing, electronics, heatsink and optics, allowing a maximum of 10 mm for the optics.
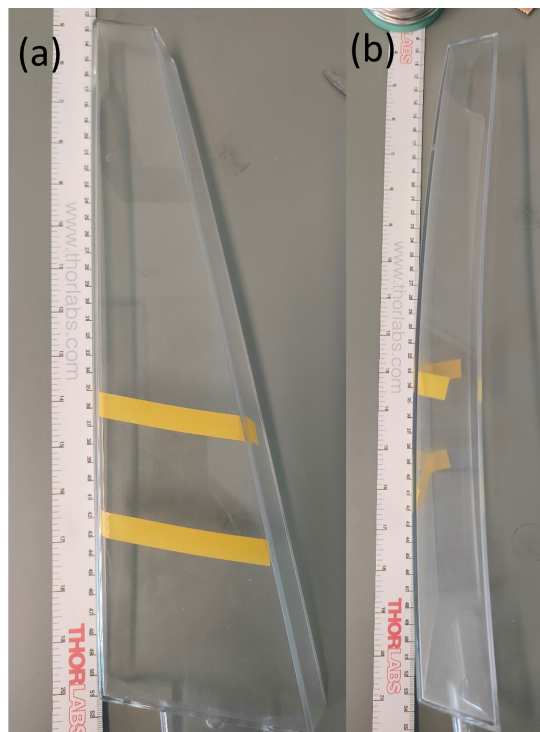
Figure 3.1: B-pillar sample used in the integration. The sample was provided by an external partner, and it is an uncoated b-pillar from a Lucid Air. Picture of the sample from (a) the front view and (b) side view.

The required FoV was derived by some experiments, using available LiDAR systems at the Hardware Team Department, searching for a solution that could achieve a minimum 2.5 meters detection distance. Figure 3.2 contains a schematic of the FoV.
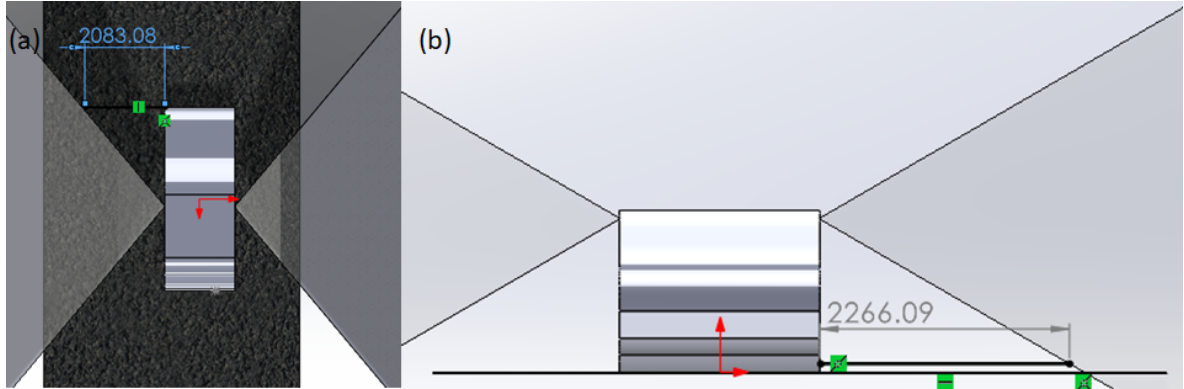
Figure 3.2: Schematic of obtained FoV from a LiDAR integrated into a b-pillar. (a) Top view of the car with the integrated LiDAR and representation of the 100° horizontal FoV. The maximum blind spot just considering this sensor and this plane is 2.083 m. (b) Front view of the car with the integrated LiDAR and representation of the 60° horizontal FoV. The maximum blind spot just considering this sensor and this plane is 2.266 m.

The experiments determined that a horizontal FoV of around 100° and vertical FoV of around 60° would meet the requirements for the application. To note here that the FoV should be higher than the field illuminated by the transmitter, to ensure that the energy reflected can be collected.

The laser used on the project is a VCSEL array working on the 905 nm wavelength. The detector chosen is a SPAD array containing 260 x 80 pixels. Each pixel has an active area of 24 µm x 24 µm and a fill factor of 45.7% as can be seen in Figure 3.3.
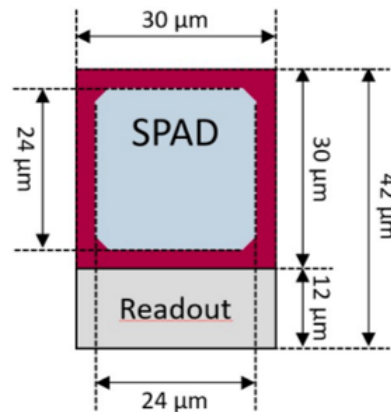
Figure 3.3: Drawing of the SPAD pixel.

Considering the chosen FoV and the number of pixels and using Equation 3.1 is possible to obtain the angular resolution limit for this combination of sensor and FoV.

$$Angular\ resolution = (\frac{FoV}{number\ of\ pixels}) \tag{3.1}$$

Using Equation 3.1 the angular resolution limit is 0.38° in one direction and 0.75° in the other. The critical case for the project is the ability to solve a 20 x 20 cm object at 20 meters distance. Using Equation 2.4, which considers the half of the size of the object as the opposite side and the distance as the adjacent side in a square triangle. Multiplying the result by a factor of two is possible to obtain the necessary resolvable angle in object space [65].

$$Object\ space\ angle\ = 2tan^{-1}(\frac{object\ size}{2 distance\ to\ object}) = 10\ mrad \qquad (3.2)$$

According to [65] the smallest resolvable image blur, the airy disk diameter, should be matched with the pixel size, using Equation 3.3. The airy disk gives a measure of the smallest feature that can be imaged by the optics.

$$Pixel\ size = Airy\ disk\ diameter = 2.44\lambda F\# \qquad (3.3)$$

Solving Equation 3.3 for the pixel size gives a F# = 10.87. This value is very large, specially when compared to the F# in other systems discussed in Chapter 2. Considering the application, where less colected light means losing laser power and consequently less system eficiency, this F# represents an upper boundary value. In [65] is stated that the angular diameter of the airy disk is related to the clear aperture diameter through Equation 2.3. The angular diameter of the airy disk gives a measure on the minimum resolvable angle in object space, accounting for diffraction limited optics.

$$Clear\ aperture\ diameter = \frac{2.44\lambda}{Angular\ diameter\ of\ Airy\ disk} = 0.22\ mm \qquad (3.4)$$

This value for clear aperture diameter sets the minimum diameter of the system. These equations set technical specification boundaries that need to be satisfied in order to be able to image the application required targets. Using Equation 2.6 the half Nyquist frequency of the sensor can be calculated, being equal to 20.83 line pairs/mm.

3.2 Design process

The optical design process can be divided in different steps. The first step is to acquire and review some system specifications (see Table 3.1). If the system has many constrains, usually is advised to find a viable a starting point, using for instance, a design with similar specifications [65].

Table 3.1: System specifications.

Requirements	Value
Total track (mm)	<10
Maximum F#	10.87
Minimum clear aperture diameter (mm)	0.22
FoV (H x V) (° x °)	100 x 60
Angular resolution (H x V) (° x °)	0.38 x 0.75
Wavelength (nm)	905
Sensor dimensions (mm x mm)	7.8 x 3.36
Pixel size (µm x µm)	24 x 24
Half Nyquist frequency of the sensor	20.83 line pairs/mm

These specifications are used as input for the computational aided programs, as Zemax OpticStudio from Ansys, OSLO from LambdaResearch or Code V from Synopsis, being these the most known. Zemax was the chosen software due to its trade-offs in price and capabilities. After setting all the inputs and system constrains obtained in the first step is necessary to select the material and the system variables, such as surface radius, aspheric coefficients, conical coefficients thickness and diameter. The next step, with all the inputs introduced, is to define a merit function with the constrains expected for the system, as well as performance indicators. The merit function calculates the error of the system when compared to the parameters inputted. Them the optimizer searches for a new solution in the variables that allows for a lower error (see Figure 3.4 (a)) [65].

On each optimization, a sanity check should be made, to be sure that the solution is heading the direction of the manufacturing constraints [65]. In Figure 3.4 (b) is available a diagram for the optical design and optimization procedure.
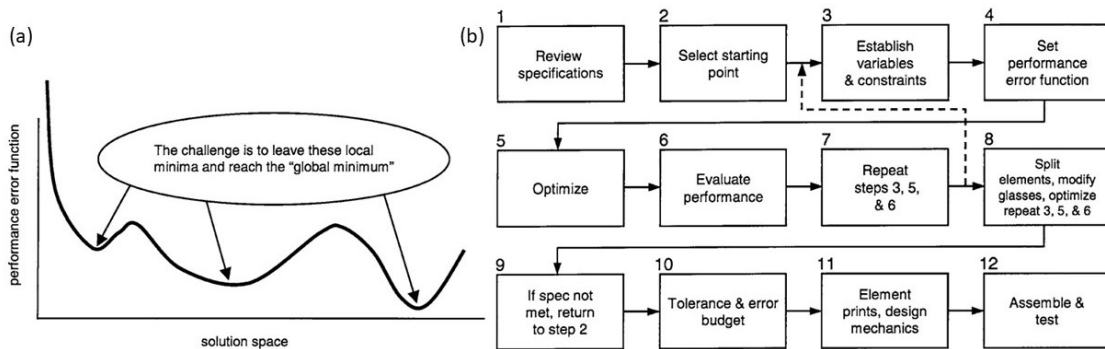
Figure 3.4: (a) Merit function error in solution space. The optimizer searches for a minimum but sometimes gets stuck in a local minimum, requiring the optical engineer to guide the solution towards the global minimum [65]. (b) Procedure for a lens design and optimization [65].

3.3 Solutions studied

The chosen starting point is a patent for a smartphone camera. It was chosen due to the compactness of the system, with a total track = 3.852 mm, a FoV of 95° and a F# = 2 [79]. The optical system described in Patent US20190129149A1 is constituted by 5 elements and a IR filter near to the image (see Figure 3.5). Looking at the materials, is noticeable that the second (element 102) and the forth (element 104) lens use materials with different index of refraction and Abbe number. These work as the cemented lens, also used in design from Figure 2.17.

The stop is located in front of the first lens to improve the image-sensing quality, as it was referred in Chapter 2. The stop at the front of the lens makes the system more telecentric, which means that the object can be imaged as at infinity. This application minimizes the chief ray hitting the image plane, which increases the light collected with a higher incidence angle [65]. The first lenses usually correct the spherical aberrations.

The last lens are highly aspherical to correct aberrations in the image sensor such as astigmatism, coma and especially, field curvature. Since the stop is located at the front is not possible to use it to balance the distortion. Usually the last two lens have a high opposite

distortion to cancel it at the image plane. To be noted that since the SPAD sensor has a dimension 3.25 bigger than the other, the maximum obtainable FoV will be different for each direction.
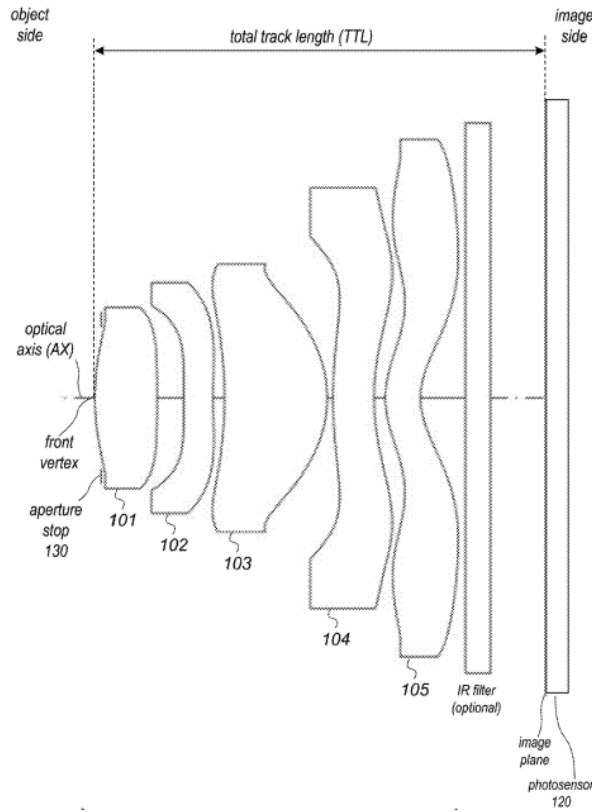
Figure 3.5: Wide angle smartphone camera design from patent US20190129149A1 [79].

The b-pillar was considered all the time in the simulations as visible in Figure 3.6. The operational temperature of the system was them defined to 60 °C. To ensure that the lens is optimized for all the FoV the field was defined using several equal area fields, covering all the area between 0° and 100° FoV. In order to reduce the number of lenses, several optimiza-
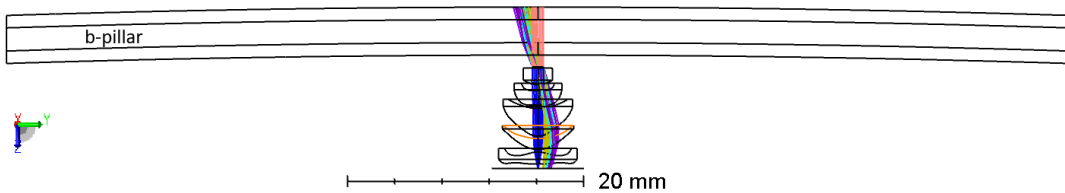
Figure 3.6: Layout of initial 5 lens system with PMMA b-pillar. The x and y axis represent the lens surface area and the z axis represents the optical axis.

tions were made, removing optical power of element 102 and element 104. After removing them, the system was scaled (having in account the dimensions of the sensor), increasing the

clear aperture diameter. After increasing the diameter, the next optimizations focus was to meet the system requirements stated in Table 3.1. The merit function searches for solutions with the minimum RMS spot size, using a damped least squares algorithm. After satisfying optimizations on the general design, several variations were made, creating solutions using PMMA and COC and varying the lens surface area.

The solutions use 3 aspheric lenses with the stop in the front. The first lens allows to collect rays in a wide FoV, with a low level of aberrations introduced. The second lens has the most optical power, noticeable in the angle of the ray bending. The level of asphericity increases in the image direction, balancing aberrations in the system. The last lens, which has a high level of asphericity, allows for the field curvature, astigmatism and distortion to be reduced.

3.3.1 Solution 1

The first solution (see Figure 3.7) uses PMMA as the optical material, which allows to decrease the manufacturing price, according to Table 2.4. In the optimization process, the variables used were the several thicknesses (lens thickness and spacing), the diameters, radius and the aspheric coefficients of the lenses. Using this optimization method allows to decrease the aberrations in the system due to more rays intercepting the image surface at the same point. Solutions are restrained in minimum and maximum thickness, but also a maximum slope for the surface angle variation, to increase the manufacturing yield of the system.
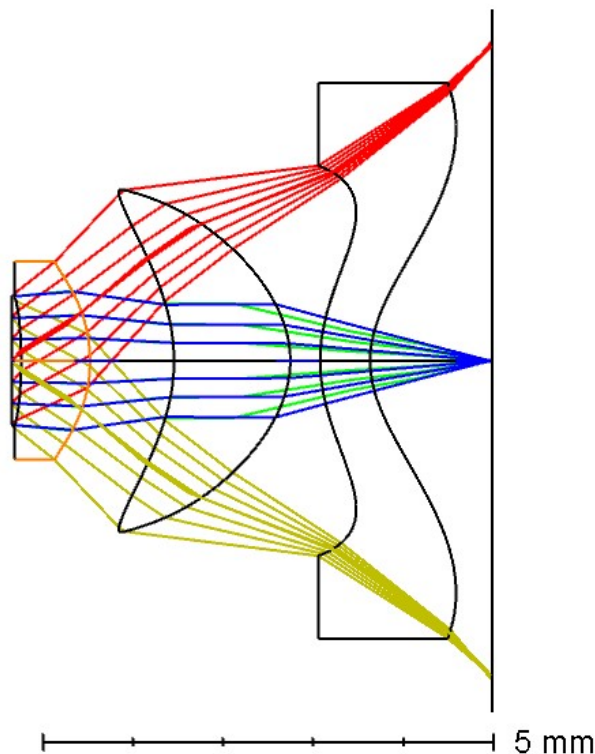
Figure 3.7: Layout of Solution 1. Representation of the 100° FoV (red rays represent +50° and yellow rays represent -50°) from stop (at left) to the image plane (at right).

The design has a F# = 1.99, maximum distortion = 1.35%. The smaller lens diameter is

1.49 mm / 2.20 mm (front surface/back surface) and the wider is 4.33 mm / 6.16 mm. The 3 lens system has a total track of 5.4 mm. Due to these, the design is very compact and exceeds the requirements in Table 3.1. According to [65] a 2.5% distortion is small enough to be imperceptible, nevertheless, can be corrected with software.

3.3.2 Solution 2

The second solution is a variation of solution 1, where instead of using PMMA the material is COC. According to [78], PMMA is difficult to coat when compared to cycloolefin polymers, as COC. Using COC increases manufacturing costs, but reduces the coating costs while achieving a higher performance than PMMA, due to better anti-reflective coatings. COC has a higher refractive index when compared to PMMA, increasing the optical power. The variation in radius from solution 1 is motivated by the change in the index of refraction from the material. The design variation has a F# = 1.97, maximum distortion = 1.41%. The smaller lens diameter is 1.49 mm / 2.26 mm (front surface/back surface) and the wider is 4.38 mm / 6.16 mm. The total track of the system is 5.5 mm.

3.3.3 Solution 3

The third solution (see Figure 3.8) is a variation of solution 2 where the clear aperture diameter was increased and consequently, the F# was decreased. Aberrations tend to increase
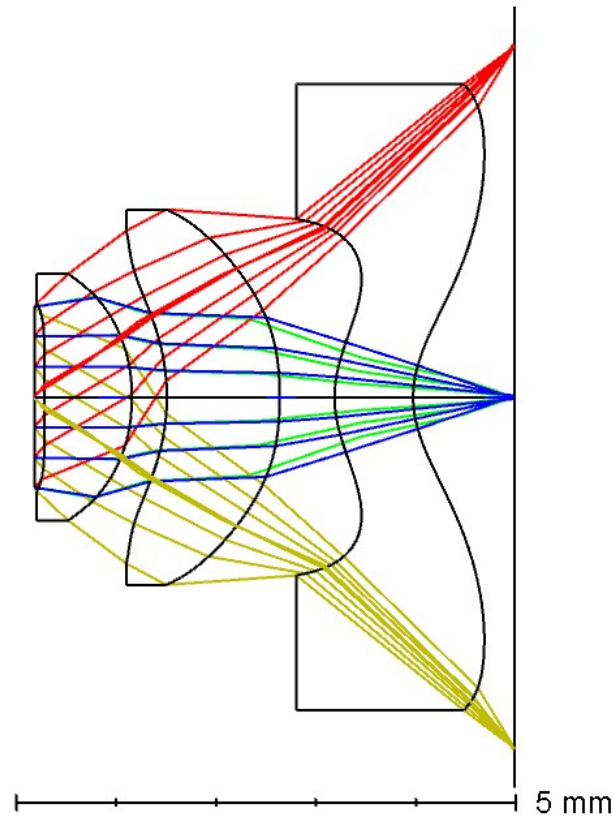
Figure 3.8: Layout of Solution 3. Representation of the 100° FoV (red rays represent +50° and yellow rays represent -50°) from stop (at left) to the image plane (at right).

with the increase of the aperture, and in this design the distortion increased when compared with the others. The design has a F# = 1.55, maximum distortion = 4.34 %. The smaller lens diameter is 2.00 mm / 2.50 mm and the widest is 8.21 mm / 7.65 mm (front surface/back surface). The total track is shorter than the first design, using 4.8 mm.

3.3.4 Performance evaluation

Solution 1 and solution 2 are very similar and therefore, behave similarly, which can be observed in Figure 3.9 (a) and Figure 3.9 (b), which represent the RMS spot size for solution 1 and 2, respectively. The off-axis imaging introduces aberrations, such as astigmatism, coma, field curvature and distortion. These increase exponentially with the increase in the incidence angle (see Table 2.2). The wide angle design poses as a challenge, requiring more computer power than regular designs, but also a higher precision when building the system, which later will be reviewed with the tolerance analysis.

Ideally, all the aberrations cancel each other. The balancing of the aberrations allows the system to cancel the sum of the aberrations. The unwanted deviated light path is deviated by other aberration, focusing it correctly. This way its possible to image with a wider FoV without introducing a significant amount of noise.

However, the system is not optimized until the diffraction limit, and the aberrations will be noticed in the RMS spot size, especially when increasing the incidence angle. In imaging applications with pixelated sensors, is preferred to have a smaller RMS spot size in a way to improve the detected photons. At the same time, a wide angle application, a optimized solution has a smaller variation between the FoV.
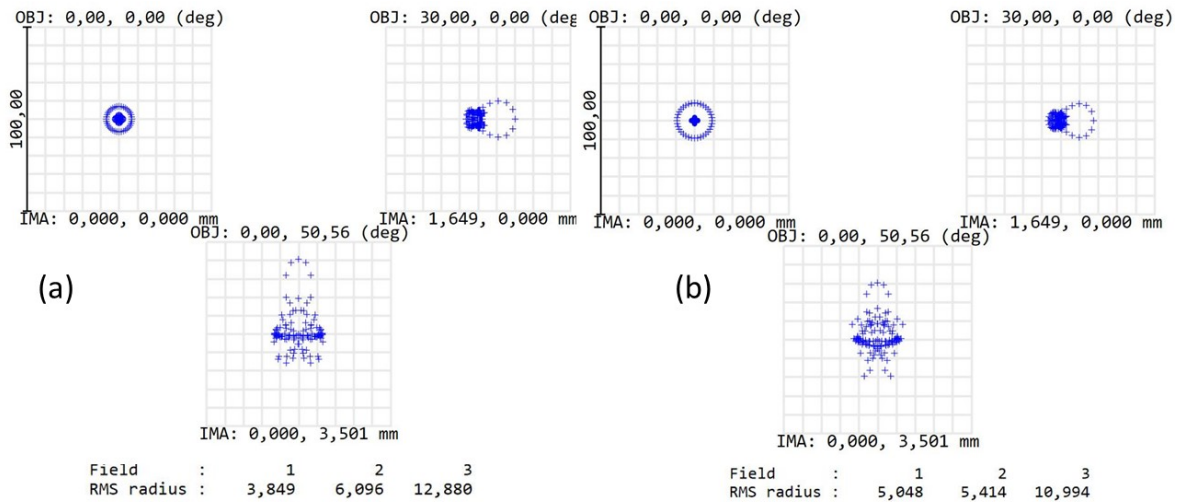
Figure 3.9: (a)The RMS spot size of solution 1 for 0°, 60° and 100° degrees incident rays. (b) The RMS spot size of solution 2 for 0°, 60° and 100° degrees incident rays. The graphic, with the title OBJ: 0,00, 0,00, represents the on-axis incidence. The OBJ: 30,00, 00 represents the incidence at 60° FoV and the OBJ: 0,00 50,56 represents the incidence at 100° FoV.

The spherical aberrations, with on-axis incidence, originates the wider circumferences surrounding the centroid area, being more noticeable in the edges of the entrance pupil. For off-axis rays, the coma and astigmatism increase, with the astigmatism being visible in the symmetric blur, and the coma visible in the asymmetric blur. Distortion also increases off-axis, but again, balancing the distortion in several surfaces with positive and negative distortion is possible to decrease it. The field curvature is mainly corrected by the field flatterner lens, the lens closest to the detector. With it high level of asphericity can correct the different focal distances from each incident angle.

Solution 2 presents a more balanced behavior between aberrations. Despite the smaller RMS radius for on-axis rays in solution 1, mainly due to a more controlled spherical aberration, the variation across FoV is higher. The astigmatism and coma in solution 1 is more noticeable than in solution 2, increasing the RMS spot size with the increase in off-axis incidence. The main difference in results between the solutions is due to the optimization level.

The RMS spot size, which contains 68% of the energy remains sub-pixel across all the FoV. This ensures that the pixels from the detector will detect the reflected laser rays. An optimization towards the diffraction limit would decrease the RMS spot size even further.

Solution 3 has a wider entrance pupil, consequently increasing the aberrations. Is easily noticiable in the 60° FoV plot in Figure 3.10 that the solution has higher astigmatism level than the other solutions. In this design a trade-off for a smaller F# , which would increase the number of photons collected, results in an higher RMS spot size. Despite remaining pixel level, the higher spot size can decrease the detected rays, decreasing the efficiency.
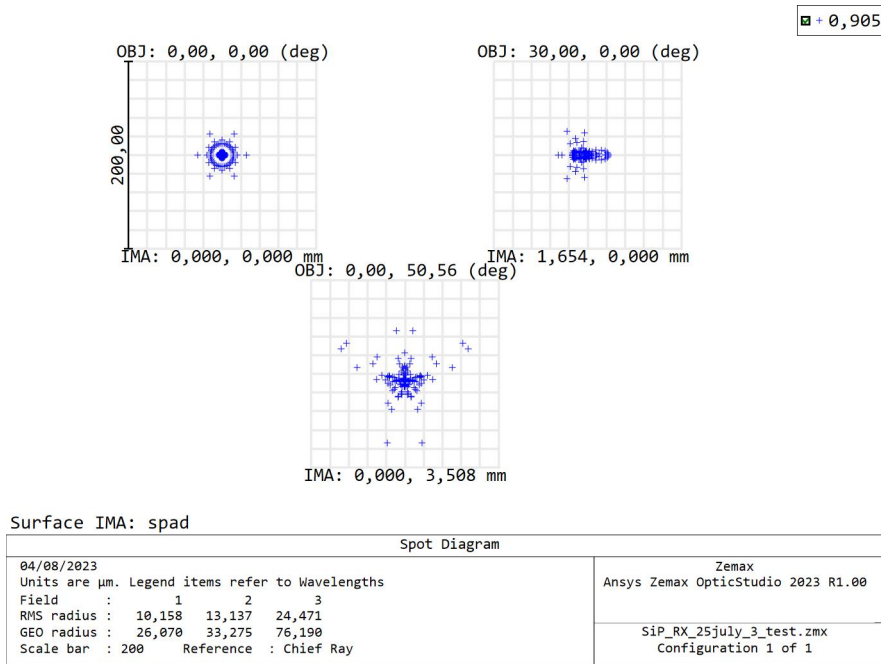
Figure 3.10: Solution 3 RMS spot size for 0°, 60° and 100° degrees incident rays.

The design is not in a fully optimized state, closer to the diffraction limit, which would balance the aberrations and decrease the spot size. The spherical aberrations are more pronounced in this solution. The spherical aberration will increase with an increase in aperture. However can be corrected with a higher level of asphericity on the first lens. The distortion

for the 3 solutions is low (see Figure 3.11), and according to [65], as already referred, can be corrected using software.
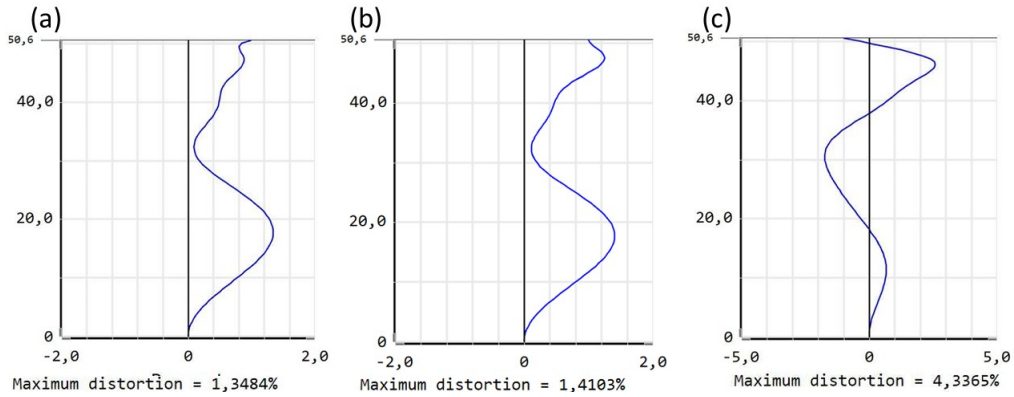
Figure 3.11: Distortion value for (a) solution 1, (b) solution 2 and (c) solution 3.

The vertical axis represents the half-incidence angle in degrees and the horizontal axis represents the distortion in percentage. Since distortion is not dependent on the aperture the higher value in solution 3 with the same incidence angle may be related with a lower level of optimization of the solution. The distortion varies along the FoV, however, the variation is very small and imperceptible.

The drop in the MTF function with the increase of the incidence angle is related to the higher number of aberrations in higher fields, as well as the light entering, which is lower for higher angles. The MTF for the sagittal plane differs from the tangential plane. This can be related to the astigmatism, the aberration where the rays from each plane have different focal lengths, especially with higher incidence angles. This is a visible effect on the MTF plots for solution 1 (see Figure 3.12), solution 2 (see Figure 3.13) and solution 3 (see Figure 3.14).
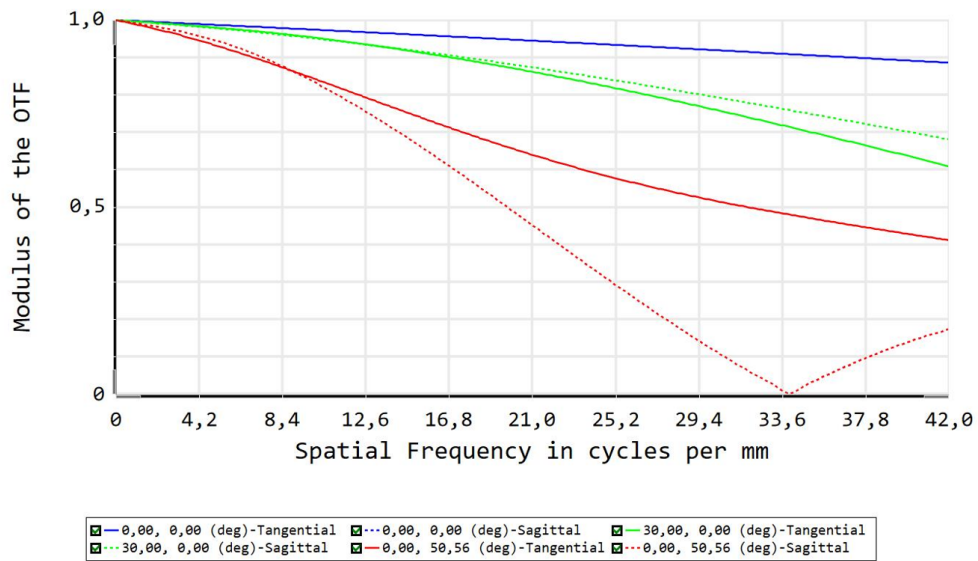
Figure 3.12: MTF function of solution 1 for 0°, 60° and 100° degrees incident rays. The vertical axis is adimensional and normalized to the maximum value.
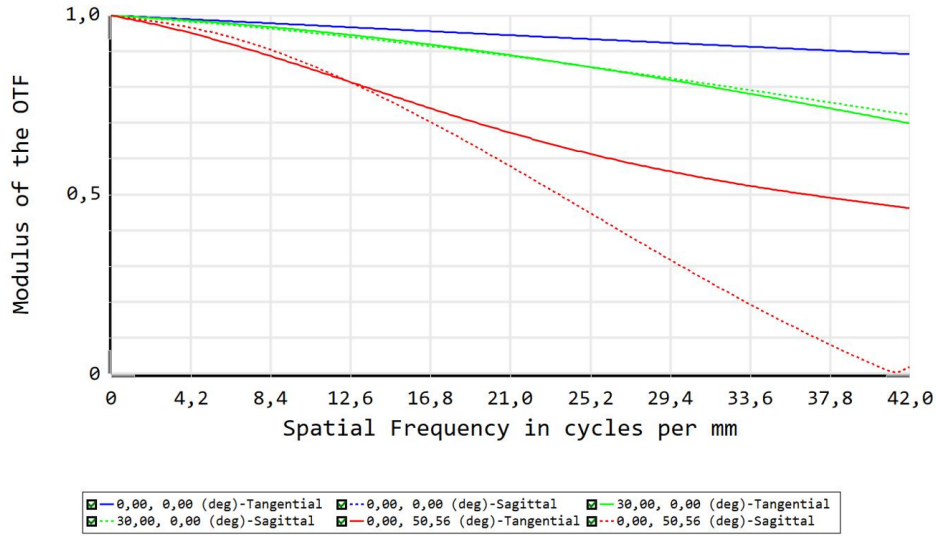
Figure 3.13: MTF function of solution 2 for 0°, 60° and 100° degrees incident rays. The vertical axis is adimensional and normalized to the maximum value.
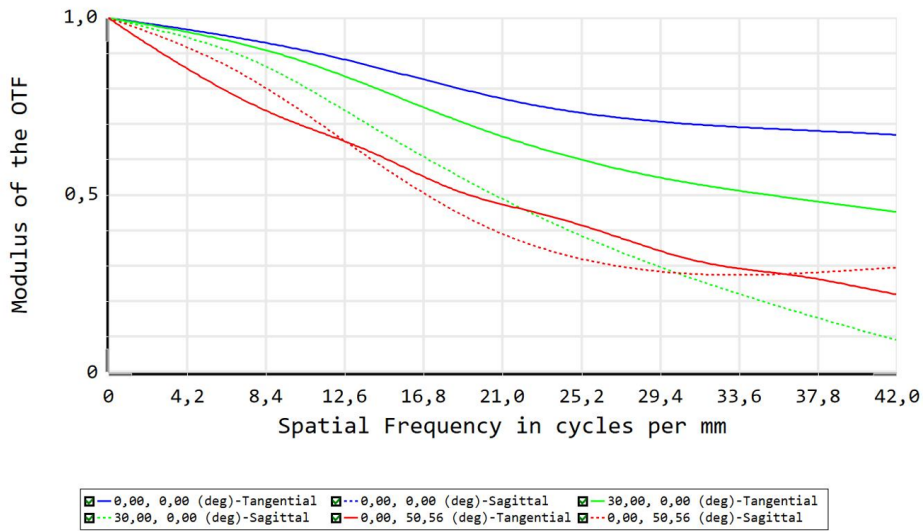
Figure 3.14: MTF function of solution 3 for 0°, 60° and 100° degrees incident rays. The vertical axis is adimensional and normalized to the maximum value.

Solution 1 and 2 suffer a sharp drop near half the Nyquist frequency at the sagittal plane for 100° FoV the MTF . With a more balanced design, where the variation of the RMS spot size is lower between angles of incidence, the contrast between the fields can also be reduced. The MTF from solution 2 also suffers a sharp drop, however the drop is already at the Nyquist frequency of the sensor, but also a much closer curve between planes for the 60° FoV. Again, the astigmatism in solution 2 is more controlled than in solution 1, reducing the gap between the curves of sagittal and tangential planes.

Solution 3 has a smaller MTF when compared to the 2 first solutions. The reduced MTF on solution 3 is a result of the higher RMS spot size. A smaller RMS spot size allows to resolve a higher frequency information with a higher contrast ratio, increasing MTF. In this case, the

RMS spot size is more affected by the aberrations, and the energy disperses into more pixels from the array. The probability of detecting the photon is then reduced, reducing the MTF and the efficiency of the system. Further optimizations of the design until a diffraction limit may balance the aberrations, reducing the spot size and consequently increasing the MTF of the solution.

Nevertheless, comparing the results with Table 2.3, the solutions remain higher than the minimum values for good imaging at half of the Nyquist frequency. Despite solution 3 reduced MTF can still be considered enough for imaging. The MTF value of the designs, will also improve if optimized until the diffraction limit. The solution with a higher MTF, due to a smaller RMS will be able to better focus the rays, collecting more energy in the detector. The decrease in the MTF translates in a smaller intensity detected in the photodetector.

Table 3.2 is a comparison chart between the 3 solutions and the main properties of the system. All the designs are able to image in the required FoV, occupying a total track lower than the maximum required by the application and with a MTF good enough for imaging. As referred before, the main difference between solution 1 and 2 is the material used, where PMMA has a smaller refractive index and its change with the temperature. Is also harder to coat with anti-reflection coatings, compared to COC. The design with the smaller total track, a critical requirement in the project, also has the widest clear aperture. The wider aperture allows to collect extra photons and improve the quality of imaging. However, the design requires further optimizations, in a way to approach it to the diffracttion limit. Since distortion only changes with the incidence angle, which is equal for all the solutions, a higher distortion value might be related to a lower optimization level.

Table 3.2: Designs comparison chart.

Specification	solution 1	solution 2	solution 3
Material	PMMA	COC	COC
Total track (mm)	5.4	5.5	4.8
F#	1.99	1.97	1.55
Clear aperture diameter (mm)	1.43	1.43	1.82
FoV (H x V) (° x °)	100 x 60	100 x 60	100 x 60
RMS Spot size (0°/60°/100°)	3.8/6.1/12.9	5/5.4/11.0	10.2/13.1/24.7
MTF 0° (%)	95	95	78
MTF 60° (sagittal/tangential)	88/86	90/90	50/68
MTF 100° (sagittal/tangential)	46/64	60/70	40/48
Maximum distortion (%)	1.35	1.4	4.34

Chapter 4

System Evaluation

4.1 Thermal analysis

The materials used can withstand the automotive temperatures, which range from -40 °C to 125 °C [80, 81]. However, when operating, the chips produce heat, reaching a more stable temperature around 60 °C. Due to that, the solutions were designed for an operational temperature of 60 °C. Nevertheless, a thermal analysis was done for the several designs. In the following subsections the variation in RMS spot size, MTF, field curvature and distortion will be analysed for -25 °C, 25 °C, 60 °C and 125 °C.

4.1.1 RMS spot size

Table 4.1, Table 4.2 and Table 4.3 summarize the change in RMS spot size with temperature for solution 1, 2 and 3, respectively. To compare the variation for the several temperatures, the relative error (Dev.) from the 60 °C value for each field is calculated in percentage.

Table 4.1: Solution 1 RMS Spot diagram for several temperatures.

Temperature/FoV	0°	Dev. (%)	60°	Dev. (%)	100°	Dev. (%)
-25 °C (µm)	3.785	-1.66	6.059	-0.61	12.708	-1.34
25 °C (µm)	3.826	-0.60	6.083	-0.21	12.850	-0.23
60 °C (µm)	3.849	0.00	6.096	0.00	12.880	0.00
125 °C (µm)	3.880	0.81	6.115	0.31	13.002	0.95

Table 4.2: Solution 2 RMS Spot diagram for several temperatures.

Temperature/FoV	0°	Dev. (%)	60°	Dev. (%)	100°	Dev. (%)
-25 °C (µm)	6.604	30.82	9.784	80.72	41.287	275.54
25 °C (µm)	5.462	8.20	6.568	21.32	22.773	107.14
60 °C (µm)	5.048	0.00	5.414	0.00	10.994	0.00
125 °C (µm)	4.452	-11.81	6.278	15.96	14.164	28.83

As expected the RMS spot size varies with the temperature. Solution 1 can be considered athermalized since there is no major variation in spot size for the different temperatures,

especially when compared to solution 2. Solution 2 has a much wider variation in spot size with the temperature, which can be in part explained by the bigger change in refractive index with variation in temperature.

Table 4.3: Solution 3 RMS Spot diagram for several temperatures.

Temperature/FoV	0°	Dev. (%)	60°	Dev. (%)	100°	Dev. (%)
-25 °C (µm)	12.159	19.70	17.283	31.56	27.064	9.51
25 °C (µm)	11.094	9.21	15.565	18.48	23.074	-6.64
60 °C (µm)	10.158	0.00	13.137	0.00	24.714	0.00
125 °C (µm)	8.740	-13.96	18.115	37.89	34.502	39.61

For solution 3, the variation is lower but still more accentuated than on solution 1. One reason for a better athermalization on solution 3 when compared to solution 2 may be the fact that system 3 has looser tolerances when compared to the solution 2. This gives the solution more degrees of freedom which translates in a better athermalization.

4.1.2 MTF

Table 4.4: Solution 1 MTF values (for sagittal/tangential planes) at half of the Nyquist frequency of the sensor for several temperatures.

Temperature/FoV	0°	60°	100°
-25 °C (%)	95	87/87	47/65
25 °C (%)	95	87/87	47/65
60 °C (%)	95	88/86	46/64
125 °C (%)	95	88/86	45/64

Table 4.5: Solution 2 MTF values (for sagittal/tangential planes) at half of the Nyquist frequency of the sensor for several temperatures.

Temperature/FoV	0°	60°	100°
-25 °C (%)	90	80/75	20/20
25 °C (%)	95	90/85	45/45
60 °C (%)	95	90/90	60/70
125 °C (%)	90	60/90	65/70

Table 4.6: Solution 3 MTF values (for sagittal/tangential planes) at half of the Nyquist frequency of the sensor for several temperatures.

Temperature/FoV	0°	60°	100°
-25 °C (%)	74	59/59	30/45
25 °C (%)	77	54/66	38/54
60 °C (%)	78	50/68	40/48
125 °C (%)	73	34/60	34/27

The MTF function of solution 1 maintains similar values for all the studied temperatures. As said before, the solution is mainly athermalized. Again, solution 2 has a higher variation

than solution 1, which can be related with the higher changes in refractive index with variation in temperature. As with the RMS spot size, solution 3 variation with temperature is lower than solution 2. Solution 2 higher lost of performance may be related in part with the higher refractive index (especially when compared with solution 1), but also due to the different sizes (especially when compared to solution 3). The small size of the optics increases the volatility of shape changes. The change in the sag of the lens causes changes in its refractive power, making it more sensitive to temperature changes. Nevertheless, all solutions maintain in the range of temperatures studied a minimum MTF value suitable for imaging.

4.1.3 Distortion

Table 4.7: Distortion value for several temperatures.

Temp	Solution 1 Max dist (%)	Solution 2 Max dist (%)	Solution 3 Max dist (%)
-25 °C	1.3464	1.5357	3.6628
25 °C	1.3477	1.4094	4.0531
60 °C	1.3484	1.4103	4.3365
125 °C	1.3493	1.9420	4.8176

Solution 1 as the smallest variation of distortion, which again proves its best athermalization. Solution 3 despite having the higher variation, from -25 °C to 60 °C, it is only 0.67%. Distortion in solution 2 varies less than is solution 3, which opposes to the RMS spot size results. One possible reason may be the fact that distortion is controlled and is not the aberration causing the image deformation. In Chapter 3, when analysing the RMS spot size for both solutions, solution 3 denoted a higher level of astigmatism, compared to the other solutions. According to the results obtained in the several simulations, the material can be used if there is a good athermalization of the design.

4.2 Tolerance analysis

The tolerance analysis is a built-in function of the design software. It uses a montecarlo algorithm to generate systems with the deviations due to manufacturing errors. These errors may lead to systems which cannot meet performance requirements. The precision values used to run the analysis are often given by a manufacturer to the designer [65].

In this thesis, the manufacturing precision values used come from the literature and are available in Table 2.5 and Table 2.6. The analysis uses the nominal value of the RMS spot size to compare the variation in performance for on-axis incidence. Table 4.8, Table 4.9 and Table 4.10 present the manufacturing tolerances for solution 1, solution 2 and solution 3, respectively, with the operators and tolerances used for each system. To simplify the reading of the tables, the several operands used in tolerancing are displayed with the following codes (x and y represent the plane parallel to the lens center) :

- tolerance on radius of curvature (TRAD)

- tolerance on thickness (TTHI)

- tolerance on element decentering in x (TEDX) and tolerance on element decentering in y (TEDY)

- tolerance on element tilting in x (TETX) and tolerance on element tilting in y (TETY)

- tolerance on index of refraction (TIND)

Table 4.8: Manufacturing tolerance analysis for solution 1.

Operand	Surface/Element	Variation (%)
TRAD (-0.15% /+0.15%)	Lens 1 front	-1.97/2.50
TRAD (-0.15% /+0.15%)	Lens 1 back	11.56/-0.61
TRAD (-0.15% /+0.15%)	Lens 2 front	86.08/75.40
TRAD (-0.15% /+0.15%)	Lens 2 back	2.31/0.17
TRAD (-0.15% /+0.15%)	Lens 3 front	1.04/-0.88
TRAD (-0.15% /+0.15%)	Lens 3 back	-0.93/1.21
TTHI (-5 µm / +5 µm)	Lens 1	55.13/33.85
TTHI (-5 µm / +5 µm)	Lens 2	7.45/6.87
TTHI (-5 µm / +5 µm)	Lens 3	1.80/-1.15
TEDX (-5 µm / +5 µm)	Lens 1 front	0.15/-0.044
TEDX (-5 µm / +5 µm)	Lens 1 back	0.16/0.13
TEDX (-5 µm / +5 µm)	Lens 2 front	-0.024/0.047
TEDX (-5 µm / +5 µm)	Lens 2 back	-0.048/0.24
TEDX (-5 µm / +5 µm)	Lens 3 front	0.013/-0.0035
TEDX (-5 µm / +5 µm)	Lens 3 back	0.029/-0.029
TEDY (-5 µm / +5 µm)	Lens 1 front	1.17/-0.90
TEDY (-5 µm / +5 µm)	Lens 1 back	-1.34/3.09
TEDY (-5 µm / +5 µm)	Lens 2 front	0.60/-0.32
TEDY (-5 µm / +5 µm)	Lens 2 back	1.47/-0.56
TEDY (-5 µm / +5 µm)	Lens 3 front	-0.29/0.37
TEDY (-5 µm / +5 µm)	Lens 3 back	-0.0082/0.013
TETX (-1 arcsec / +1 arcsec)	Lens 1 front	1.09/-0.95
TETX (-1 arcsec / +1 arcsec)	Lens 1 back	-0.70/0.80
TETX (-1 arcsec / +1 arcsec)	Lens 2 front	-0.11/0.16
TETX (-1 arcsec / +1 arcsec)	Lens 2 back	0.54/-0.34
TETX (-1 arcsec / +1 arcsec)	Lens 3 front	-0.089/0.92
TETX (-1 arcsec / +1 arcsec)	Lens 3 back	0.031/-0.031
TETY (-1 arcsec / +1 arcsec)	Lens 1 front	0.011/0.0056
TETY (-1 arcsec / +1 arcsec)	Lens 1 back	-0.035/-0.0048
TETY (-1 arcsec / +1 arcsec)	Lens 2 front	-8.6309E-07/1.0699E-06
TETY (-1 arcsec / +1 arcsec)	Lens 2 back	0.070/-0.033
TETY (-1 arcsec / +1 arcsec)	Lens 3 front	0.0008/-0.0008
TETY (-1 arcsec / +1 arcsec)	Lens 3 back	-0.011/0.010
TIND (-0.001 / +0.001)	Lens 1	-3.72/6.45
TIND (-0.001 / +0.001)	Lens 2	5.16/9.85
TIND (-0.001 / +0.001)	Lens 3	0.63/-0.563

The analysis allows to understand where the precision should be focused when manufacturing and assembling the systems. From the data in Table 4.8 is possible to conclude that the radius variation on the front surface of the second lens, is the error that affects this

system the most. Similar results are observed in solution 2, again, with the highest offender the variation in radius for the first surface of the second lens.

Table 4.9: Manufacturing tolerance analysis for solution 2.

Operand	Surface/Element	Variation (%)
TRAD (-0.15% /+0.15%)	Lens 1 front	-2.14/2.87
TRAD (-0.15% /+0.15%)	Lens 1 back	14.14/-2.41
TRAD (-0.15% /+0.15%)	Lens 2 front	89.12/102.17
TRAD (-0.15% /+0.15%)	Lens 2 back	1.73/1.13
TRAD (-0.15% /+0.15%)	Lens 3 front	1.19/-1.00
TRAD (-0.15% /+0.15%)	Lens 3 back	-1.14/1.40
TTHI (-5 µm / +5 µm)	Lens 1	53.73/22.80
TTHI (-5 µm / +5 µm)	Lens 2	6.33/9.10
TTHI (-5 µm / +5 µm)	Lens 3	1.94/-1.18
TEDX (-5 µm / +5 µm)	Lens 1 front	6.56/4.77
TEDX (-5 µm / +5 µm)	Lens 1 back	13.73/13.29
TEDX (-5 µm / +5 µm)	Lens 2 front	0.50/1.19
TEDX (-5 µm / +5 µm)	Lens 2 back	8.30/11.40
TEDX (-5 µm / +5 µm)	Lens 3 front	0.65/0.34
TEDX (-5 µm / +5 µm)	Lens 3 back	0.34/-0.28
TEDY (-5 µm / +5 µm)	Lens 1 front	22.19/3.85
TEDY (-5 µm / +5 µm)	Lens 1 back	47.44/81.78
TEDY (-5 µm / +5 µm)	Lens 2 front	17.41/2.70
TEDY (-5 µm / +5 µm)	Lens 2 back	50.31/33.09
TEDY (-5 µm / +5 µm)	Lens 3 front	-0.36/7.93
TEDY (-5 µm / +5 µm)	Lens 3 back	-0.08/0.46
TETX (-1 arcsec / +1 arcsec)	Lens 1 front	0.03/-0.03
TETX (-1 arcsec / +1 arcsec)	Lens 1 back	-0.02/0.02
TETX (-1 arcsec / +1 arcsec)	Lens 2 front	-0.02/0.02
TETX (-1 arcsec / +1 arcsec)	Lens 2 back	0.05/-0.05
TETX (-1 arcsec / +1 arcsec)	Lens 3 front	-0.008/0.008
TETX (-1 arcsec / +1 arcsec)	Lens 3 back	0.004/-0.004
TETY (-1 arcsec / +1 arcsec)	Lens 1 front	0.0003/-0.0003
TETY (-1 arcsec / +1 arcsec)	Lens 1 back	0.0006/-0.0006
TETY (-1 arcsec / +1 arcsec)	Lens 2 front	-0.001/0.001
TETY (-1 arcsec / +1 arcsec)	Lens 2 back	0.004/-0.004
TETY (-1 arcsec / +1 arcsec)	Lens 3 front	0.0008/-0.0008
TETY (-1 arcsec / +1 arcsec)	Lens 3 back	-0.001/0.001
TIND (-0.001 / +0.001)	Lens 1	-3.30/6.38
TIND (-0.001 / +0.001)	Lens 2	1.60/10.92
TIND (-0.001 / +0.001)	Lens 3	0.57/-0.52

To ensure a proper performance for the second lens of both solutions, the precision fabricating it must be higher, while requiring to be measured more often to ensure that the sag of the surfaces are manufactured according to the design. The precision in centering and tilting may be lowered for all the lens in both solutions.

Is possible to conclude that for both systems, tolerances in the last lens may be lowered, as the precision in centering and tilting, in order to reduce costs. The material used to produce the second lens requires to have a higher precision in its index of refraction.

Table 4.10: Manufacturing tolerance analysis for solution 3.

Operand	Surface/Element	Variation (%)
TRAD (-0.15% /+0.15%)	Lens 1 front	-0.017/0.017
TRAD (-0.15% /+0.15%)	Lens 1 back	-0.66/1.65
TRAD (-0.15% /+0.15%)	Lens 2 front	9.66/-4.53
TRAD (-0.15% /+0.15%)	Lens 2 back	-0.37/0.43
TRAD (-0.15% /+0.15%)	Lens 3 front	-1.46/1.65
TRAD (-0.15% /+0.15%)	Lens 3 back	1.78/-1.37
TTHI (-5 µm / +5 µm)	Lens 1	2.33/3.21
TTHI (-5 µm / +5 µm)	Lens 2	6.40/-2.72
TTHI (-5 µm / +5 µm)	Lens 3	0.002/0.42
TEDX (-5 µm / +5 µm)	Lens 1 front	15.78/9.56
TEDX (-5 µm / +5 µm)	Lens 1 back	6.43/12.93
TEDX (-5 µm / +5 µm)	Lens 2 front	1.84/2.10
TEDX (-5 µm / +5 µm)	Lens 2 back	1.78/2.75
TEDX (-5 µm / +5 µm)	Lens 3 front	0.98/-0.13
TEDX (-5 µm / +5 µm)	Lens 3 back	-0.14/0.28
TEDY (-5 µm / +5 µm)	Lens 1 front	15.57/10.27
TEDY (-5 µm / +5 µm)	Lens 1 back	16.33/0.66
TEDY (-5 µm / +5 µm)	Lens 2 front	6.36/3.38
TEDY (-5 µm / +5 µm)	Lens 2 back	7.09/42.29
TEDY (-5 µm / +5 µm)	Lens 3 front	13.65/-4.06
TEDY (-5 µm / +5 µm)	Lens 3 back	0.51/-0.38
TETX (-1 arcsec / +1 arcsec)	Lens 1 front	-0.01/0.01
TETX (-1 arcsec / +1 arcsec)	Lens 1 back	0.01/-0.01
TETX (-1 arcsec / +1 arcsec)	Lens 2 front	0.009/-0.009
TETX (-1 arcsec / +1 arcsec)	Lens 2 back	-0.04/0.04
TETX (-1 arcsec / +1 arcsec)	Lens 3 front	0.009/-0.009
TETX (-1 arcsec / +1 arcsec)	Lens 3 back	-0.004/0.004
TETY (-1 arcsec / +1 arcsec)	Lens 1 front	-0.001/0.001
TETY (-1 arcsec / +1 arcsec)	Lens 1 back	0.005/-0.005
TETY (-1 arcsec / +1 arcsec)	Lens 2 front	-0.001/0.001
TETY (-1 arcsec / +1 arcsec)	Lens 2 back	0.002/-0.002
TETY (-1 arcsec / +1 arcsec)	Lens 3 front	-0.001/0.001
TETY (-1 arcsec / +1 arcsec)	Lens 3 back	0.001/-0.001
TIND (-0.001 / +0.001)	Lens 1	2.79/-0.95
TIND (-0.001 / +0.001)	Lens 2	4.89/-3.31
TIND (-0.001 / +0.001)	Lens 3	0.10/-0.10

As the previous solutions, the second lens is the one suffering a higher variation in performance with the radius tolerance and refractive index. Since in all the solutions is the lens with the higher refractive power, is expected for all the solutions that the change in radius or

refractive index returns a higher change in performance.

Solution 3 suffers smaller variations of performance with the same tolerances as the other solutions. This can be related with its bigger size, which for the same tolerances allows a lower precision. Contrary to other solutions, the worst offender is the decentering tolerance for the second lens. The decentering of the second lens affects the light entering the third lens which corrects most of the aberrations. The tolerance analysis before the manufacturing and assembling allows to predict the behavior of the systems with the introduced manufactured errors. If a system requires higher precision, the manufacturing will use the precision required, saving on unusable systems. At the same time, if a system requires lower precision to meet the requirements, the precision can be decreased, decreasing the manufacturing costs.

Table 4.11, Table 4.12 and Table 4.13 present the assembling tolerances for solution 1, solution 2 and solution 3, respectively.

Table 4.11: Assembling tolerance analysis for solution 1.

Operand	Surface/Element	Variation (%)
TTHI (-5 µm / +5 µm)	Stop to lens 1 gap	50.79/40.28
TTHI (-5 µm / +5 µm)	Lens 1 to lens 2 gap	35.47/42.91
TTHI (-5 µm / +5 µm)	Lens 2 to lens 3 gap	-1.32/1.73
TTHI (-5 µm / +5 µm)	Lens 3 to SPAD gap	-2.58/3.89
TEDX (-5 µm / +5 µm)	Lens 1	0.23/0.011
TEDX (-5 µm / +5 µm)	Lens 2	-0.013/0.35
TEDX (-5 µm / +5 µm)	Lens 3	0.042/-0.033
TEDY (-5 µm / +5 µm)	Lens 1	-0.52/1.85
TEDY (-5 µm / +5 µm)	Lens 2	2.51/-0.40
TEDY (-5 µm / +5 µm)	Lens 3	-0.29/0.39
TETX (-1 arcsec / +1 arcsec)	Lens 1	0.016/-0.015
TETX (-1 arcsec / +1 arcsec)	Lens 2	0.0069/-0.0067
TETX (-1 arcsec / +1 arcsec)	Lens 3	-0.0035/0.0035
TETY (-1 arcsec / +1 arcsec)	Lens 1	0.00094/-0.00092
TETY (-1 arcsec / +1 arcsec)	Lens 2	0.0005/-0.00048
TETY (-1 arcsec / +1 arcsec)	Lens 3	-0.00011/0.00011

As in manufacturing tolerances, solution 1 and 2 present similar results. The error on the thickness of the first lens or the distance from it to the stop or the second lens also introduces a higher degradation to the system performance. When mounting the first two lens the distance precision should also be higher allowing for a higher margin for mechanical errors. Since these lens have a higher refractive power and deal with higher incidence angles require more precision when mounting.

During the assembling the tilting and centering tolerances can be lowered, due to the minimal changes in performance. The similar results are mainly due the similar sags and thickness of both systems. The variation is higher in solution 2 due to the higher refractive index material. With more refractive power, the same change in sag creates a higher change in the direction of the rays exiting the lens.

The worst offender in the assembling process for all the solutions is the distance between lens, especially the distance between the aperture stop and the first lens but also the distance from the first lens to the second. This result may derive from the small focal length of all the

systems. Unfocusing the first two lens affects rays with wider angles, which cannot correctly focus and drop the system performance.

Table 4.12: Assembling tolerance analysis for solution 2.

Operand	Surface/Element	Variation (%)
TTHI (-5 µm / +5 µm)	Stop to lens 1 gap	50.01/28.10
TTHI (-5 µm / +5 µm)	Lens 1 to lens 2 gap	23.56/42.69
TTHI (-5 µm / +5 µm)	Lens 2 to lens 3 gap	-1.31/1.82
TTHI (-5 µm / +5 µm)	Lens 3 to SPAD gap	-2.83/4.53
TEDX (-5 µm / +5 µm)	Lens 1	0.24/-0.01
TEDX (-5 µm / +5 µm)	Lens 2	-0.05/0.37
TEDX (-5 µm / +5 µm)	Lens 3	0.05/-0.04
TEDY (-5 µm / +5 µm)	Lens 1	-1.20/2.44
TEDY (-5 µm / +5 µm)	Lens 2	3.27/-1.26
TEDY (-5 µm / +5 µm)	Lens 3	-0.43/0.52
TETX (-1 arcsec / +1 arcsec)	Lens 1	0.03/-0.03
TETX (-1 arcsec / +1 arcsec)	Lens 2	0.008/-0.008
TETX (-1 arcsec / +1 arcsec)	Lens 3	-0.004/0.004
TETY (-1 arcsec / +1 arcsec)	Lens 1	0.001/-0.001
TETY (-1 arcsec / +1 arcsec)	Lens 2	0.0007/-0.0007
TETY (-1 arcsec / +1 arcsec)	Lens 3	-0.0001/0.0001

**Table 4.13:** Assembling tolerance analysis for solution 3.

Operand	Surface/Element	Variation (%)
TTHI (-5 µm / +5 µm)	Stop to lens 1 gap	-3.00/13.57
TTHI (-5 µm / +5 µm)	Lens 1 to lens 2 gap	8.39/-3.43
TTHI (-5 µm / +5 µm)	Lens 2 to lens 3 gap	0.61/-0.39
TTHI (-5 µm / +5 µm)	Lens 3 to SPAD gap	-1.30/-0.63
TEDX (-5 µm / +5 µm)	Lens 1	0.06/0.01
TEDX (-5 µm / +5 µm)	Lens 2	-0.009/0.12
TEDX (-5 µm / +5 µm)	Lens 3	0.04/-0.03
TEDY (-5 µm / +5 µm)	Lens 1	1.28/-1.11
TEDY (-5 µm / +5 µm)	Lens 2	-1.83/2.30
TEDY (-5 µm / +5 µm)	Lens 3	1.00/-0.90
TETX (-1 arcsec / +1 arcsec)	Lens 1	-0.0007/0.0007
TETX (-1 arcsec / +1 arcsec)	Lens 2	0.008/-0.008
TETX (-1 arcsec / +1 arcsec)	Lens 3	0.005/-0.005
TETY (-1 arcsec / +1 arcsec)	Lens 1	0.0005/-0.0005
TETY (-1 arcsec / +1 arcsec)	Lens 2	-0.0003/0.0003
TETY (-1 arcsec / +1 arcsec)	Lens 3	0.0002/-0.0002

The assembly centering and tilting tolerances results for solution 3 are also similar to the first two solutions since this system allows for this tolerances to be lowered. Solution 3 however, has lower variation with the same tolerances applied, as in manufacturing. This result can again be related to the bigger size of the system.

Despite having a smaller variation with the tolerance analisys, solution 3 has a wider RMS spot size. The smaller variation of performance with the same tolerances makes the manufacturing of the system more cost-effective, because more systems will have the expected performance.

At the same time another tolerance study may reveal easier tolerances for this system, making its manufacturing and assembling cheaper than the others, which already suffer a substantial variation in performance with these tolerance values.

Figure 4.1 is a graphic representation of the RMS spot size (µm) plotted against the yield (%). All the possible systems for each design, created with the fluctuations in manufacturing and assembly are considered. The graphic allows to compare the behavior of the RMS spot size with the tolerances for all the solutions, where ideally the solutions would have a step function near the Yield axis.
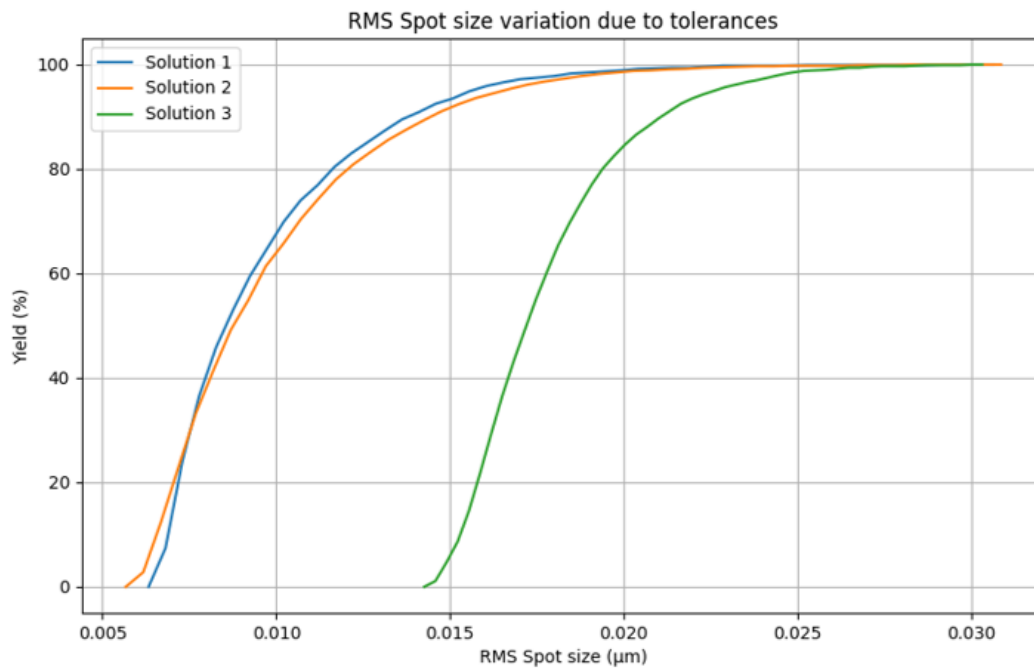
Figure 4.1: Resulting tolerance RMS spot size with manufactured yield (%). The yield represents the amount of manufactured systems with the considered tolerances.

The results from the previous tables corroborate the results in Figure 4.1. The design with the smaller variation in performance from the tables, suffers a smaller change in RMS spot size for the same yielded systems. 80% of Design 3 produce a RMS spot size close to the expected, while for the other designs more than doubled.

But, despite a higher variation in RMS spot size, solution 1 and 2 have smaller spot size, which allows for higher fluctuations in the system. At the same time, the yielded solutions for the first two solutions remain pixel-level considering the tolerance deviations.

4.3   Results analysis

The solutions presented above suffer from aberrations such as spherical aberration, astigmatism, coma and distortion. Solution 1 and 2 are identical with the main difference, the material. Solution 1 is designed in PPMA, while solution 2 is in COC. PPMA as a lower refractive index, but it variation with temperature is also lower. COC is easier to coat with anti-reflection coatings than PMMA. The coating is essential to assure the performance of the optical system.

Solution 2 shows a more balanced behavior between aberrations, which is related to a higher level of optimization of the solution during modelling. This behavior can be related with a higher level of optimization. Solution 3 has a wider entrance pupil, which inherently will increase the aberrations. However, an optimization in which the level of aberrations is balanced in a way to cancel each other is possible.

The RMS spot size of solution 3 is wider than pixel size and has a higher distortion level. The MTF values for all the solutions are considered good for imaging, but to be noted that solution 1 and 2 have higher values than solution 3. Solution 3 has a smaller focal length and a wider clear aperture, allowing it to collect more photons.

Figure 4.2 and Figure 4.3 represent in a histogram the amount of tolerance operands that have a change in performance inferior to 5%, between 5% and 20% and above than 20%, for manufacturing and assembling, respectively. Table 4.14 summarizes and compares the results of the thermal analysis and the manufacturing and assembling tolerances with the higher change in performance.
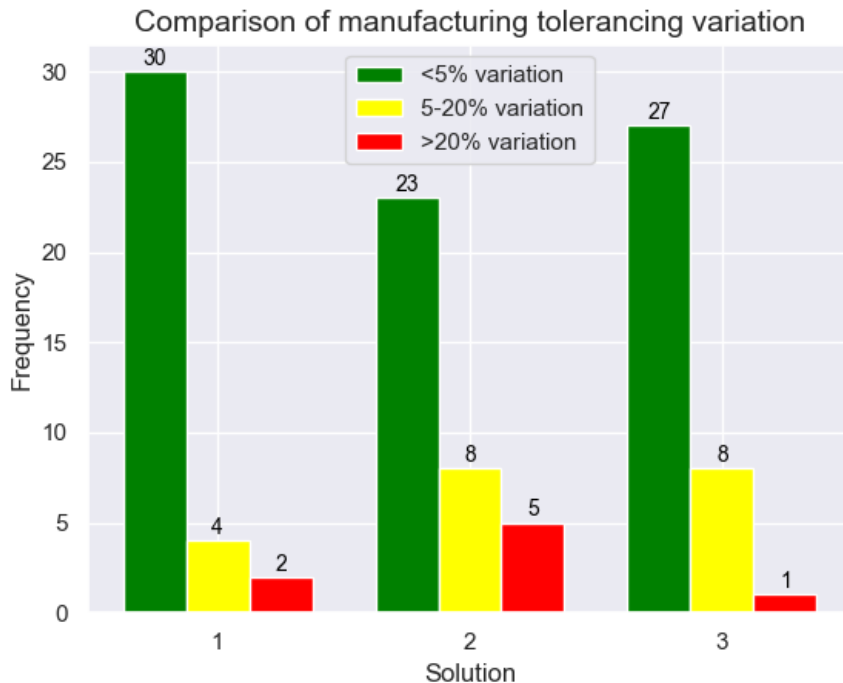
Figure 4.2: Histogram with manufacturing tolerances for the 3 solutions. To categorize the data was sorted by the performance variation as indicated in the label.
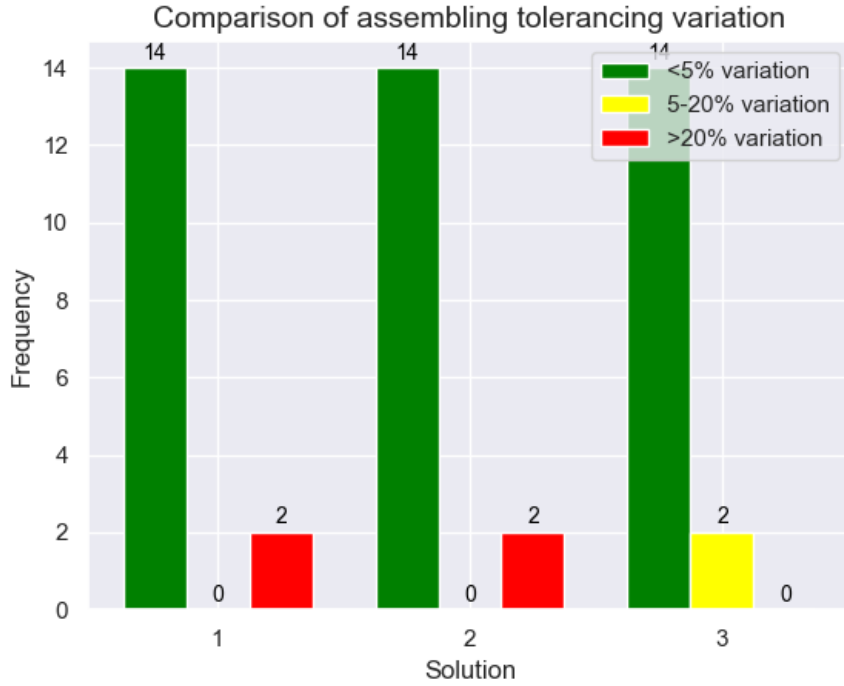
Figure 4.3: Histogram with assembling tolerances for the 3 solutions. To categorize the data was sorted by the performance variation as indicated in the label.

Table 4.14: Summary of the results obtained (TRAD (tolerance on radius of curvature), TTHI (tolerance on thickness) and TEDY (tolerance on element decentering)).

Specification	solution 1	solution 2	solution 3
Athermalization	Good	Fair	Good
Manuf. worst offenders var. (operator)	86.08% (TRAD)	102.17% (TRAD)	42.29% (TEDY)
Assem. worst offenders var. (operator)	50.79% (TTHI)	50.01% (TTHI)	13.57% (TTHI)

In the previous sections the tolerances were analised for all the designs, concluding that solution 1 and 2 require more precision in manufacturing and assembling than solution 3. Observing the data in Figure 4.2 and Figure 4.3 is noticeable that solution 3 has a better performance than the others.

The smaller size of the optics will create bigger changes in performance with the same precision applied. In all the systems the more sensitive lens to manufacture is the second lens, which has the higher refractive power and bends the wider incidence angles. In the assembling the position of the first lens, is what creates higher fluctuations in the system. If this lens is out of focus, all the rays entering the system will be displaced.

Solution 1 is the solution with less variation due to the temperature. Since solution 1 uses PMMA with the lower refractive index, but also suffers less variation of it due to the temperature is natural that this solution is less affected than solution 2. At the same time, solution 3 is constituted from the same material, but has a smaller variation than solution 2. This result may be explained by the looser tolerances of the last design. Since the solution is less prone to suffer a decrease in performance due to changes in the distance between lens

allows it to work better in a wide range of temperatures.

Solution 1 and 2, which showed better results in RMS spot size and MTF and remain sub-pixel during all the FoV, may be better optimized than solution 3. Depending on the available manufacturer with its precision these solutions might be a viable point. If the manufacturer cannot produce lens with such a precision, then an approach as solution 3, with a scaled system, allows to reduce the precision needed when tolerancing for manufacturing.

Chapter 5

Conclusion and future work

The work on this thesis was a good contribution for the company, opening new understandings in viable products of interest for the company. The objective of this work was to design a miniaturized optical system for an automotive LiDAR application. The application has several boundary conditions. To be able to integrate the sensor in the b-pillar of the car, its optical system needs to be less than 10 mm of thickness. The FoV for the system was determined as 100° and 60° for horizontal and vertical orientation. The laser set the working wavelength and the SPAD detector set the pixel and array dimensions.

The design approach was to use a smartphone design patent as a starting point, allowing to reduce the system volume without compromising its performance. Smartphone designs are very compact solutions which use lenses with a high level of asphericity, decreasing their volume while mantaining performance. Three designs were modulated at a temperature of 60 °C using Zemax, in a way to evaluate the performance of the system.

The designs comprise a 3 aspheric lenses system. Decreasing the number of lens in the system decreases complexity and price. At the same time, since there is less tolerances associated with the manufacturing and mounting process, the system is less prone to perturbations affecting performance. Solution 1 and 2 are identical in design, with the former optimized for PMMA and latter in COC. PMMA has a lower index of refraction change with temperature than COC and is more cost-effective, however it is harder to coat with anti-reflection coatings. Solution 3 is a variation using COC with a wider clear aperture and smaller focal length, allowing to decrease its F#, increasing the light entering the photodetector.

Solution 1 and 2 have better RMS and MTF values when compared to solution 3. Nevertheless, the systems meet the requirements established by the several boundary conditions. A thermal study was also conducted, where the solutions proved to be able to withstand the automotive temperatures. Solution 2 was the most affected solution, which in part can be related to its higher change in the index of refraction with temperature, when compared to solution 1. When compared to solution 3 its smaller diameter and aperture can be the reason for the higher change with temperature.

A tolerances study was conducted in a way to evaluate the system performance with errors introduced by manufacturing and assembling processes. The tolerances analysis revealed that solution 3 can be produce with lower tolerances than the other systems, which may be related to the bigger size of the lens. The lens that requires the highest precision in all systems is the second lens, which has a highest refractive power. The precision in the tilting and decentration for all the systems can be lowered in order to reduce the costs.

If the manufacturer is capable of coating the PMMA and manufacturing the system with the suggested tolerances, solution 1 is the more viable solution. If the manufacturer is not capable of coating it efficiently or cost-effectively the other solutions might be more viable. According to the thermal analysis, solution 2 will perform worst than solution 3 when exposed to different temperatures. The manufacturing and assembling tolerances are significantly lower on solution 3. On the other hand, solution 3 yielded worst RMS spot size and MTF results than solution 2 with more pronounced aberrations. Solution 2 and 3 present a trade-off between a smaller F# or a smaller spot size (and consequently aberrations and MTF). However, these aberrations may be decreased with a higher level of optimization of the solution until a sub-pixel state of the RMS spot size. This work can be advanced by two main points of focus: first a feasibility study for manufacturing, and second a detailed study on spectral variation with temperature.

A first step would be re-optimize the suggested design even further. After a performance check on the software, a next work will be to manufacture the design and compare the differences between the simulations and the manufactured system. The feasibility study can include the tolerances and precision of the process used by the manufacturer and the tolerances for assembly in the production line of the LiDAR system. Another interesting point for future work is to input cost-effective tolerances given by manufacturers and redesign the system with those inputs, in a way to decrease the manufacturing and assembling costs.

To further increase the reliability of the simulation, a study on the source spectrum variation with the temperature variation can be done. This would ensure that the working wavelength of the systems was matched with the source.

In addition, to increase performance a new optical design could include the use of micro lenses in the detector array itself. This will result in lower losses due to fill-factor of the pixel and higher absorption in the photodetector by decreasing the incident angle [82].

Bibliography

[1] E. Parliament, "Road fatality statistics in the EU (infographic)." 6 October 2021, [Online]. Available: `https://www.europarl.europa.eu/news/en/headlines/society/20190410STO36615/road-fatality-statistics-in-the-eu-infographic`, accessed 2023-02-16.

[2] S. Raviteja and R. Shanmughasundaram, "Advanced driver assitance system (adas)," in *2018 Second International Conference on Intelligent Computing and Control Systems (ICICCS)*, pp. 737–740, 2018.

[3] Synopsys, "What is an autonomous car." [Online]. Available: `https://www.synopsys.com/automotive/what-is-autonomous-car.html`, accessed 2023-02-16.

[4] R. Wessel, "A brief history of the cruise control system in your car." 30 March 2022, [Online]. Available: `https://www.tomtom.com/newsroom/explainers-and-insights/a-brief-history-of-cruise-control-systems/`, accessed 2023-02-16.

[5] D. Gibson, "What is ABS? Anti-lock brake systems explained." 23 September 2020, [Online]. Available: `https://www.autoexpress.co.uk/car-news/98072/what-is-abs-anti-lock-brake-systems-explained/`, accessed 2023-02-16.

[6] Hyundai, "The evolution of cruise control." 30 May 2018, [Online]. Available: `https://www.hyundai.news/eu/articles/stories/the-evolution-of-cruise-control.html/`, accessed 2023-02-18.

[7] U. Roskoni, "Monitoring the blind spot.." [Online]. Available: `https://www.continental-automotive.com/getattachment/380ab13f-6c07-4e7a-a210-9517ec00bb30/Continental_RightViu_Technical-Articel_EN.pdf.pdf/`, accessed 2023-02-19.

[8] B. Gmbh, "Lane departure warning." [Online]. Available: `https://www.bosch-mobility.com/en/solutions/assistance-systems/lane-departure-warning/`, accessed 2023-02-18.

[9] Valeo, "Park4u® automated parking." [Online]. Available: `https://www.valeo.com/en/park4u-automated-parking/`, accessed 2023-02-18.

[10] A. Shaout, D. Colella, and S. Awad, "Advanced driver assistance systems - past, present and future," in *2011 Seventh International Computer Engineering Conference (ICENCO'2011)*, pp. 72–82, 2011.

[11] S. Campbell, N. O'Mahony, L. Krpalcova, D. Riordan, J. Walsh, A. Murphy, and C. Ryan, "Sensor technology in autonomous vehicles : A review," in *2018 29th Irish Signals and Systems Conference (ISSC)*, pp. 1–4, 2018.

[12] C. Rablau, "Lidar: a new self-driving vehicle for introducing optics to broader engineering and non-engineering audiences," in *Fifteenth Conference on Education and Training in Optics and Photonics: ETOP 2019* (A.-S. Poulin-Girard and J. A. Shaw, eds.), vol. 11143, p. 111430C, International Society for Optics and Photonics, SPIE, 2019.

[13] P. Wang, "Research on comparison of lidar and camera in autonomous driving," *Journal of Physics: Conference Series*, vol. 2093, p. 012032, nov 2021.

[14] K. Ramasubramanian and K. Ramaiah, "Moving from legacy 24 ghz to state-of-the-art 77-ghz radar," *ATZelektronik worldwide*, vol. 13, pp. 46–49, Jun 2018.

[15] S. Fidler, "Depth from stereo - lecture 12." 2015, [Online]. Available: `http://www.cs.toronto.edu/~fidler/slides/2015/CSC420/lecture12_hres.pdf`, accessed 2023-02-19.

[16] S. Royo and M. Ballesta-Garcia, "An overview of lidar imaging systems for autonomous vehicles," *Applied Sciences*, vol. 9, no. 19, 2019.

[17] M. E. Newman, "To the Moon and Back ... in 2.5 Seconds." 13 February 2019, [Online]. Available: `https://www.nist.gov/nist-time-capsule/any-object-any-need-call-nist/moon-and-back-25-seconds`, accessed 2023-02-19.

[18] B. Allen, "Lidar atmospheric sensing experiment (lase):measuring water vapor, aerosols and clouds." NASA, 22 April 2008, [Online]. Available: `https://www.nasa.gov/centers/langley/news/factsheets/LASE.html`, accessed 2023-02-20.

[19] E. Simley, L. Y. Pao, N. Kelley, B. Jonkman, and R. Frehlich, "Lidar wind speed measurements of evolving wind fields," *Conference: Presented at the 50th AIAA Aerospace Sciences Meeting Including the New Horizons Forum and Aerospace Exposition, 9-12 January 2012, Nashville, Tennessee, United States of America*, 1 2012.

[20] S. E. Johnson, W. C. Haneberg, L. S. Bryson, and M. M. Crawford, "Measuring ground surface elevation changes in a slow-moving colluvial landslide using combinations of regional airborne lidar, UAV lidar and UAV photogrammetric surveys," *Quarterly Journal of Engineering Geology and Hydrogeology*, vol. 56, pp. qjegh2022–078, 03 2023.

[21] Businesswire, "Global automotive lidar market analysis and forecast report 2023: A $3.1 billion market by 2028 from $555 million in 2022 - rising demand for autonomous vehicles/increasing sales of electric vehicles - researchandmarkets.com." 07 April 2023, [Online]. Available: `https://www.businesswire.com/news/home/20230407005055/en/Global-Automotive-LIDAR-Market-Analysis-and-Forecast-Report-2023-A-3.1-Billion-Market-by-2028-from-555-Million-in-2022`, accessed 2023-05-10.

[22] M.-C. Amann, T. M. Bosch, M. Lescure, R. A. Myllylae, and M. Rioux, "Laser ranging: a critical review of unusual techniques for distance measurement," *Optical Engineering*, vol. 40, no. 1, pp. 10 – 19, 2001.

[23] V. Ilci and C. Toth, "High definition 3d map creation using gnss/imu/lidar sensor integration to support autonomous vehicle navigation," *Sensors*, vol. 20, p. 899, Feb 2020.

[24] N. Jayaweera, N. Rajatheva, and M. Latva-aho, "Autonomous driving without a burden: View from outside with elevated lidar," in *2019 IEEE 89th Vehicular Technology Conference (VTC2019-Spring)*, pp. 1–7, 2019.

[25] Y. Li, L. Ma, Z. Zhong, F. Liu, M. A. Chapman, D. Cao, and J. Li, "Deep learning for lidar point clouds in autonomous driving: A review," *IEEE Transactions on Neural Networks and Learning Systems*, vol. 32, no. 8, pp. 3412–3432, 2021.

[26] L. Willems, *Understanding the Impacts of Autonomous Vehicles in Logistics*, ch. 8, pp. 113–127. John Wiley & Sons, Ltd, 2021.

[27] B. G. Alisson Sarmento *et al.*, "The autonomous vehicle challenges for emergent market," *SAE Technical Paper 2017-36-0436*, 2017.

[28] H. Flämig, *Autonomous Vehicles and Autonomous Driving in Freight Transport*, pp. 365–385. Berlin, Heidelberg: Springer Berlin Heidelberg, 2016.

[29] H. Holzhüter, "The autonomous vehicle challenges for emergent market," *EPIC Online Technology Meeting on ADAS and Autonomous Driving*, 2020.

[30] G. A. Kumar, J. H. Lee, J. Hwang, J. Park, S. H. Youn, and S. Kwon, "Lidar and camera fusion approach for object distance estimation in self-driving vehicles," *Symmetry*, vol. 12, p. 324, Feb 2020.

[31] A. Broggi, "Latest challenges in autonomous vehicles: A practitioner's perspective: Technology leadership brief," *SAE Technical Paper 2012-01-9018*, 2012.

[32] J. B. Charlie Gates *et al.*, "Noise, vibration, and harshness considerations for autonomous vehicle perception equipment," *SAE Int. J. Adv. & Curr. Prac. in Mobility*, vol. 2, no. 3, pp. 1382–1389, 2020.

[33] H. Fountain, "Yes, driverless cars know the way to san jose." 26 October 2012, [Online]. Available: `https://www.nytimes.com/2012/10/28/automobiles/yes0driverless-cars-know-the-way-to-san-jose.html`, accessed 2023-06-14.

[34] C. Bellanger, "They tried the autonomous zoe cab. here is what they have to say." 18 November 2019, [Online]. Available: `https://www.renaultgroup.com/en/news-on0air/news/they-tried-the-autonomous-zoe-cab-here-is-what-they-have-to-say/`, accessed 2023-06-29.

[35] Edmunds, "B pillar)." [Online]. Available: `https://www.edmunds.com/glossary/b-pillar.html`,.

[36] W. by AGC, "Wideye® by agc to display lidar sensor mounted in b-pillar at autosens show in brussels."
9 July 2022, [Online]. Available: `https://www.agc-glass.eu/en/news/press-release/wideye-agc-d isplay-lidar-sensor-mounted-b-pillar-autosens-show-brussels`, accessed 2023-07-05.

[37] P. Mcmanamon, P. Banks, J. Beck, D. Fried, A. Huntington, and E. Watson, "Comparison of flash lidar detector options," *Optical Engineering*, vol. 56, p. 031223, 03 2017.

[38] R. Roriz, J. Cabral, and T. Gomes, "Automotive lidar technology: A survey," *IEEE Transactions on Intelligent Transportation Systems*, vol. 23, no. 7, pp. 6282–6297, 2022.

[39] N. Li, C. P. Ho, J. Xue, L. W. Lim, G. Chen, Y. H. Fu, and L. Y. T. Lee, "A progress review on solid-state lidar and nanophotonics-based lidar sensors," *Laser & Photonics Reviews*, vol. 16, no. 11, p. 2100511, 2022.

[40] J. Dinan, "Using solid-state flash lidar technology to access better and lower-cost vehicle profiling data in e-tolling applications," *LeddarTech*, 2020.

[41] J. Skidmore, "Semiconductor lasers for 3-d sensing," *Optics & Photonics News Magazine February 2019 Issue*, vol. 30, 2019.

[42] H. Mönch, "Vertical-cavity surface-emitting lasers: Vcsel arrays provide leading-edge illumination for 3d sensing." 12 October 2017, [Online]. Available: `https://www.laserfocusworld.com/lasers-sources/a rticle/16548239/verticalcavity-surfaceemitting-lasers-vcsel-arrays-provide-leadingedge-i llumination-for-3d-sensing`, accessed 2023-07-05.

[43] X. Sun, L. Zhang, Q. Zhang, and W. Zhang, "Si photonics for practical lidar solutions," *Applied Sciences*, vol. 9, p. 4225, Oct 2019.

[44] W. Brune, "Meteo 300: Fundamentals of atmospheric science: The solar spectrum." A. Dutton Institute for Teaching and Learning Excellence, [Online]. Available: `https://www.e-education.psu.edu/meteo30 0/node/683`, accessed 2023-07-01.

[45] J. Wojtanowski, M. Zygmunt, M. Kaszczuk, Z. Mierczyk, and M. Muzal, "Comparison of 905 nm and 1550 nm semiconductor laser rangefinders' performance deterioration due to adverse environmental conditions," *Opto-Electronics Review*, vol. 22, no. 3, pp. 183–190, 2014.

[46] T. Ghosh, "Why gaas and iii-vs probably won't replace silicon." 28 December 2018, [Online]. Available: `https://medium.com/@sixsamuraisoldier/why-gaas-and-iii-vs-probably-wont-replace-silicon -568b4701901d.`, accessed 2023-07-08.

[47] U. Wafer, "Silicon (si) vs germanium (ge) substrate compared." [Online]. Available: `https://www.univ ersitywafer.com/silicon-vs-germanium.html`, accessed 2023-07-08.

[48] A. Carrasco-Casado and R. Mata-Calvo, *Space Optical Links for Communication Networks*, pp. 1057–1103. Cham: Springer International Publishing, 2020.

[49] Hexagon—Autonomoustuff, "Lidar comparison chart." [Online]. Available: `https://autonomoustuff.c om/lidar-chart`, accessed 2023-06-29.

[50] MicroVision, "Movia lidar sensor." [Online]. Available: `https://microvision.com/products/movia-l idar-sensor`, accessed 2023-06-29.

[51] O. Inc., "Ds0 short-range." [Online]. Available: `https://ouster.com/products/ds0-sensor/`, accessed 2023-06-29.

[52] elmos, "Optical sensors - lidar." 2023, [Online]. Available: `https://www.elmos.com/fileadmin/elmos-w ebsite/landing-pages/virtual-booth/documents/elmos-lidar-tof-2023.pdf`, accessed 2023-06-29.

[53] A. S. C. LLC, "Gsfl-16k 3d flash lidar™ camera." [Online]. Available: `https://asc3d.com/gsfl_16k/`, accessed 2023-07-01.

[54] H. L. S. AG, "Technical data lissa universal industrial." [Online]. Available: `https://www.hybrid-lid ar.com/assets/2022-05-24_datasheet_lissa_industrie.pdf`, accessed 2023-07-01.

[55] H. L. S. AG, "Leddar™ pixell." [Online]. Available: `https://leddartech.com/app/uploads/dlm_uploa ds/2021/04/Spec-Sheet_Leddar-Pixell_V7.0_EN.pdf`, accessed 2023-07-01.

[56] Toyo, "Xenolidar." [Online].

[57] N. Corporation, "Plano-concave lenses." [Online]. Available: `https://www.newport.com/c/plano-conca ve-lenses`, accessed 2023-07-01.

[58] N. Corporation, "Build to order transmission diffraction gratings." [Online]. Available: `https://www.newport.com/g/custom-plane-transmission-gratings`, accessed 2023-07-01.

[59] Focuslight, "Wide-angle diffuser (wad)." [Online]. Available: `https://focuslight-www.oss-ap-southeast-1.aliyuncs.com/wp-content/uploads/2022/09/Focuslight_Wide-Angle-Diffuser.pdf`, accessed 2023-07-01.

[60] G. G. Gimmestad and D. W. Roberts, *Lidar Engineering: Introduction to Basic Principles.* Cambridge University Press, 2023.

[61] T. Inc, "N-bk7 plano-concave lenses, uncoated." [Online]. Available: `https://www.thorlabs.com/newgrouppage9.cfm?objectgroup_id=2087`, accessed 2023-07-01.

[62] Z. Mor, "Integrated structured-light projector." United States of America Patent US9740019B2, 22 08 2017.

[63] T. Inc, "Nir transmission gratings." [Online]. Available: `https://www.thorlabs.com/newgrouppage9.cfm?objectgroup_id=178`, accessed 2023-07-01.

[64] X. F. Neil MacKinnon, Weiping Li, "Top-emission vcsel-array with integrated diffuser." United States of America Patent US20170370554A1, 28 December 2017.

[65] R. E. Fischer, B. Tadic-Galeb, and P. R. Yoder, *Optical system design.* SPIE Press, 2008.

[66] E. Hecht, *Optik.* Berlin, Boston: De Gruyter, 2018.

[67] Ansys, "Opticstudio user manual." 2023.

[68] J. E. Greivenkamp, *Field guide to geometrical optics.* SPIE Press, 2004.

[69] J. Sasián, *Introduction to Lens Design.* Cambridge University Press, 2019.

[70] J. Bentley and C. Olson, *Retrofocus and Wide-Angle Lenses.* 2012.

[71] K. Mizuguchi, "Fisheye lens." United States of America Patent US6844991B2, 05 02 2002.

[72] V. Blahnik and O. Schindelbeck, "Smartphone imaging technology and its applications," *Advanced Optical Technologies*, vol. 10, no. 3, pp. 145–232, 2021.

[73] T.-C. K. Cheng-Chen Lin, Yu-Tai TSENG, "Optical photographing lens assembly, image capturing unit and electronic device." United States of America Patent US20160341937A1, 19 January 2021.

[74] H.-H. H. Tsung-Han Tsai, "Optical image capturing system." United States of America Patent US20160341937A1, 24 November 2016.

[75] I. Y. Park, "Optical imaging system." United States of America Patent US10317645B2, 31 May 2018.

[76] H.-H. H. Tsung-Han Tsai, "Optical image capturing system." United States of America Patent US10890740B2, 26 March 2020.

[77] A. Z. R. N. Youngworth, *Review of Optical Manufacturing 2000 to 2020.* SPIE / International Society for Optical Engineering, 2021.

[78] U. Schulz, "Review of modern techniques to generate antireflective properties on thermoplastic polymers," *Appl. Opt.*, vol. 45, pp. 1608–1618, Mar 2006.

[79] Y. Yao, "Wide field of view five element lens system." United States of America Patent US20190129149A1, 2 May 2019.

[80] C. T. Committee, "Failure mechanism based stress test qualification for optoelectronic semiconductors in automotive applications," April 2020.

[81] TOPAS, "Cyclic olefin copolymer (coc)." [Online]. Available: `https://www-eng.lbl.gov/~shuman/NEXT/CURRENT_DESIGN/TP/FO/COC_topas_product-brochure_english.pdf`, accessed 2023-08-16.

[82] Hamamatsu, "Microlens arrays." [Online]. Available: `https://hamamatsu.magnet.fsu.edu/articles/microlensarray.html`,.